THE ASTROPHYSICAL JOURNAL, 652:1626–1653, 2006 December 1

EVOLUTION OF THE CIRCUMSTELLAR MOLECULAR ENVELOPE. I. A BIMA CO SURVEY OF EVOLVED STARS

D. FONG,[1,2] M. MEIXNER,[1,3] E. C. SUTTON,[1] A. ZALUCHA,[1,4] AND W. J. WELCH[5]
Received 2003 March 10; accepted 2006 August 1

ABSTRACT

This paper reports the results of a small imaging survey of eight evolved stars including two AGB stars (IRC +10216 and Mira), five proto–planetary nebula (PPN) candidates (AFGL 2688, IRAS 22272+5435, HD 161796, 89 Her, and HD 179821), and a planetary nebula (PN, NGC 7027). We present high-resolution ^{12}CO $J = 1 \rightarrow 0$ maps of their full molecular envelopes made by combining BIMA Millimeter Array and NRAO 12 m telescope observations. For the PPNe and PN, the neutral molecular envelopes are compared with images taken at optical, near-IR, and mid-IR wavelengths. Drawing from the literature, we augmented our BIMA survey sample to 38 well-studied sources with CO emission maps. We classified this sample of sources based on the kinematics and morphologies of the CO emission into three types: spherical/elliptical/shell sources, disk sources, and structured outflow sources. Confirming previous studies, we find strong evidence for the photodissociation of the molecular envelope as an object evolves from the AGB to PN stages. While the spherical AGB stars follow theoretical expectations for mass-loss rate versus envelope size, the post-AGB structured outflow sources have significantly higher mass-loss rates than expected probably because of their recent superwinds. We find evidence that the structured outflows are clearly younger than the AGB wind. The disk sources have little correlation between mass-loss rate and envelope size because their properties are determined more by the properties of the central stars and disk evolution than by the mass-loss rate history that shapes the spherical and structured-outflow sources.

Subject headings: circumstellar matter — radio lines: stars — stars: AGB and post-AGB — stars: mass loss

1. INTRODUCTION

The evolution of an asymptotic giant branch (AGB) star is driven by mass loss. It loses a large fraction of its mass in a low-velocity wind (10–20 km s^{-1}) that forms an extensive envelope of gas and dust. This phase is thought to end with a burst of mass loss that ejects most of the remaining envelope of the star into the circumstellar environment. The star then progresses to warmer $T_{\rm eff}$ in a short transitional, proto–planetary nebula (PPN) phase. As the central star becomes hotter, the molecular envelope will be photodissociated and then photoionized, thus forming a planetary nebula (PN). At some point during the PPN phase, fast winds will start to develop with velocities 10–100 times faster than the previously ejected AGB wind, driving shocks into the circumstellar envelope (CSE). In addition to radiative and shock-driven changes, the spherical AGB envelope dramatically transforms into an axisymmetric PN.

The hydrodynamic models of PN formation are inspired by the two-dimensional (2D) projected structures observed in optical images of PNe (Balick & Frank 2002). Optical imaging surveys of PNe (e.g., Balick 1987; Manchado et al. 1996; Sahai & Trauger 1998) reveal round, elliptical, bipolar, and multipolar morphologies. Optical and mid-infrared imaging surveys of PPNe reveal bipolar (aka DUPLEX/core elliptical) and elliptical (aka SOLE/toroidal) types (Ueta et al. 2000; Meixner et al. 1999b). However, the kinematic information on these sources is less well known, but it is critical for understanding the dramatic change in morphology between the AGB and PN stages. The best method to obtain the kinematic information from the AGB to PPN stages is to measure the CO emission arising from the molecular gas. In fact, molecular gas measurements provide a continuous link from the AGB to PPN to PN that reveals the evolution of the morphological and kinematical structures through these stages. Furthermore, the CO line emission allows the entire molecular envelope to be probed since CO, through self-shielding, is very resistant to photodissociation. In addition, CO is the best tracer of the nebular mass in the AGB and PPN stages.

In contrast to the optical surveys of PN, CO surveys inherently provide kinematic information; however, until recently, morphological information has been missing. The majority of CO observations have been conducted using single-dish telescopes (e.g., Knapp & Morris 1985; Olofsson et al. 1993; Bujarrabal et al. 2001), with few observations showing fully resolved structures (see the compilation by Loup et al. 1993). For all but the nearest and most extended objects, interferometer observations are needed to resolve the circumstellar envelopes. Crude estimates of the mass-loss rate can be derived with a single spectrum (e.g., Knapp & Morris 1985). With high-resolution, full synthesis maps of the entire molecular envelope, the full mass-loss history of the circumstellar molecular gas is revealed. Neri et al. (1998) conducted the largest single-dish and interferometric snapshot survey of 46 AGB and post-AGB stars, revealing that the morphologies of most of the sources are roughly spherical. Exactly when and how this disruption from spherical symmetry to axial symmetry emerges is not well understood. However, the origin and the behavior of the late−AGB to post-AGB mass loss appear to be different from the AGB mass loss. A CO line survey of 32 PPNe by Bujarrabal et al. (2001) showed that, in the majority of their sources, the post-AGB winds exhibit much higher velocities than the AGB winds and that these fast outflows may be collimated along axial directions.

[1] Astronomy Department, University of Illinois, 1002 West Green Street, Urbana, IL 61801.
[2] Harvard-Smithsonian Center for Astrophysics, 645 A'ohoku Place, Hilo, HI 96720.
[3] Space Telescope Science Institute, 3700 San Martin Drive, Baltimore, MD 21218.
[4] Department of Earth, Atmospheric, and Planetary Sciences, Massachusetts Institute of Technology, 77 Massachusetts Avenue, Cambridge, MA 02139.
[5] Department of Astronomy, University of California, 601 Campbell Hall, Berkeley, CA 94720.

TABLE 1
Source Properties

Source	Alternate Names	R.A. (J2000.0)	Decl. (J2000.0)	V_{LSR} (km s^{-1})	Evol/Chem
IRC +10216	CW Leo, IRAS 09452+1330	09 47 57.36	+13 16 43.60	−26.0	AGB/C
Mira	IRAS 02168−0312, *o* Ceti	02 19 20.79	−02 58 26.30	+47.0	AGB/O
IRAS 22272+5435	HD 235858	22 29 10.29	+54 51 06.60	−27.5	PPN/C
HD 179821	AFGL 2343, IRAS 19114+0002	19 13 58.53	+00 07 31.60	+99.0	PPN/O
AFGL 2688	Egg Nebula	21 02 18.75	+36 41 37.80	−35.0	PPN/C
HD 161796	IRAS 17436+5003	17 44 55.43	+50 02 38.40	−33.8	PPN/O
89 Her	IRAS 17534+2603	17 55 25.10	+26 02 58.60	−8.0	PPN/O
NGC 7027		21 07 01.71	+42 14 10.06	+26.0	PN/C

Note.— Units of right ascension are hours, minutes, and seconds, and units of declination are degrees, arcminutes, and arcseconds.

In order to increase our knowledge of the morphology and kinematics of the molecular gas, we have pursued high-quality, full synthesis maps to accurately image both the small- and large-scale CO emission in eight evolved stars. The focus of this survey is to investigate the morphological and kinematical transformation of the molecular AGB envelope in its transition to a PN.

The remainder of this paper is organized as follows. In § 2 we detail the interferometric and single-dish observations and describe our technique for combining the data sets. In § 3 we present the data via channel maps, spectra, and position-velocity diagrams for each source. We discuss in detail the morphologies and kinematics and compare the results with images taken at other wavelengths in the context of their evolutionary stages. In § 4 we present a classification of sources based on the kinematics and morphologies of the CO emission. The classification is based on an enlarged sample of 38 objects that includes the Berkeley-Illinois-Maryland-Association (BIMA) survey with augmentation of similar data from the literature. In § 5 we discuss the radiative and kinematical evolutions of the molecular envelope. In § 6 we summarize our conclusions.

2. OBSERVATIONS

We observed eight evolved stars using both the BIMA[6] Millimeter Array and the NRAO[7] 12 m telescope in the ^{12}CO $J = 1 \rightarrow 0$ line transition at 115.2712 GHz. The NRAO 12 m was used to recover extended emission. For the spatially compact sources, the 12 m observations were used as a check to determine if all of the flux had been recovered by the BIMA observations. For IRC +10216, a full description of the BIMA and NRAO 12 m on-the-fly observations is provided in Fong et al. (2003). Table 1 lists the eight evolved stars in order of their evolutionary age. Half of the objects are carbon-rich (C-rich, C/O $>$ 1), and the other half are oxygen-rich (O-rich, C/O $<$ 1). In Table 1 we list the right ascension, declination, and evolutionary status/chemical type.

2.1. *BIMA Observations*

Interferometric observations were made with the 10-element BIMA array at Hat Creek, California (Welch et al. 1996). The observational details of each source are listed in Table 2 with the observation dates, array configurations, and (u, v) ranges given in columns (2)–(4), respectively. The array configurations used in the observations span from the most compact configuration "D array" to the extended configuration "B array." A single pointing was used for the smaller sources, while multiple pointing/mosaicked observations were conducted for the more extended objects. Column (5) lists the number of pointings and the field of view. The instrumental and atmospheric phase variations were calibrated against quasars (col. [6]), and the absolute flux calibration was determined from observations of planets (col. [7]). The 1 σ uncertainty to the flux calibration is about 20% (Regan et al. 2001). For all of the sources, the correlator was configured to cover a bandwidth of 50 MHz, resulting in a velocity coverage of 128 km s^{-1} with a spectral resolution of 1 km s^{-1}. Data reduction

[6] Operated by the University of California, Berkeley, the University of Illinois, and the University of Maryland, with support from the National Science Foundation.
[7] The National Radio Astronomy Observatory is a facility of the National Science Foundation operated under cooperative agreement by Associated Universities, Inc.

TABLE 2
BIMA Observing Parameters

Source (1)	Date (2)	Array (3)	UV Range (kλ) (4)	Number of Points/FOV HPBW (arcsec) (5)	Calibrators: Phase/Amp (6)	Calibrators: Flux (7)	T_{sys} (K) (8)
IRC +10216	1999 Aug–1999 Nov	D[a]	2.3–11.2	19/280	0909+013	Venus	400–1200
Mira	1998 Apr–1999 Aug	C,[a] D	2.3–31.0	7/160	0238+166	Venus, Jupiter	400–1200
IRAS 22272+5435	1998 Apr–2001 Jun	B, C	2.3–91.4	1/100	BLLAC	Venus, Mars	300–1200
HD 179821	1998 May–2000 Mar	B, C, D[a]	2.3–91.3	7/160	1751+096	Venus, Mars, Uranus	400–1200
AFGL 2688	1998 Apr–2001 Jun	B,[a] C, D	2.3–91.4	7/160	BLLAC, 2013+370	Venus, Mars, Neptune	300–1000
HD 161796	1998 Apr–2001 Jun	B,[a] C, D	2.4–87.3	1/100	3C 345	Venus, Mars, Neptune	300–1200
89 Her	2001 Jun–2002 Feb	B, C, D[a]	2.3–82.0	1/100	1751+096	Uranus, Neptune	300–1200
NGC 7027	1998 Apr–2001 Jun	C, D	2.3–31.0	7/190	2013+370	Venus, Neptune	300–1200

[a] Multiple tracks observed in this array configuration.

TABLE 3
NRAO 12 m Observing Parameters

Source	Grid Size (arcmin)	Grid Spacing (arcsec)	Off Position (arcmin)	T_{sys} (K)
IRC +10216	8 × 8	on-the-fly	20 RA	400–800
Mira	7 × 7	22	4 AZ	400–900
IRAS 22272+5435	6 × 5	22	5 RA	300–500
HD 179821	5 × 5	22	4 AZ	400–1000
AFGL 2688	7 × 7	22	5 AZ	400–1000
HD 161796	5 × 5	22	4 AZ	300–500
89 Her	. . .	. . .	. . .	. . .
NGC 7027	9 × 9	22	5 AZ	300–600

was performed in the MIRIAD software package (Sault et al. 1995). Standard data reduction, calibration, imaging and deconvolution procedures were followed. The data were self-calibrated to remove the residual phase errors. Self-calibration improved the image quality by about 10%. We carefully inspected the final images so as not to introduce artifacts. Self-calibration was not performed on Mira because it did introduce low-level artifacts. The remaining maps including all of the mosaic pointings showed improvement after self-calibration. Robust weighting was applied to the visibility data to produce the dirty images.

2.2. *NRAO* 12 m *Observations*

Single-dish data were obtained during 1999 February using the NRAO 12 m telescope at Kitt Peak, Arizona. The observations were conducted using position switched mode, where on-source integration times of 30 s were followed by 30 s integrations off-source. Pointing was monitored every few hours with observations of planets. The details of the observations are listed in Table 3. All of the sources were observed with dual polarizations using two 128 channel filter banks with a spectral resolution of 0.5 MHz (1.3 km s^{-1}). The absolute flux calibration at the 12 m is accurate to within 10%. Data reduction was performed in the NRAO UNIPOPS software package. Standard procedures for flagging, baseline removal, combining scans, and mapping were followed.

2.3. *BIMA and NRAO* 12 m *Data Combination*

The AGB stars, PPNe, and PN in our sample range in angular extent from 10″ to nearly 400″. The most extended emission provides valuable information on the earlier epochs of mass loss; thus, mapping the entire molecular envelope is necessary to create an accurate model of the mass-loss history. With a single pointing, interferometer observations are only sensitive to the region in the sky covered by the primary beam. In addition, an interferometer is sensitive to spatial frequencies set by the maximum and minimum separations of the antenna elements. The minimum separation determines the response to large-scale structure. For BIMA, extended emission with spatial scales larger than ~40″ will be increasingly resolved out (Helfer et al. 2002). To observe emission that is much larger than the primary beam, mosaicking observations are required. However, for each field in the mosaic, about the same range of spatial frequencies as in the single pointing will be detected. Thus, the low spatial frequency information that globally unites the separate fields together will still be missing. For a mosaic, by using all of the *uv* information in the separate fields together through a "joint deconvolution" technique (Sault et al. 1996), lower spatial frequency information can be partially recovered. However, in order to recover all of the flux, single-dish data must be combined with the interferometer data.

We have investigated several methods for combining interferometer and single-dish data for our data sets. The two data sets can be combined in the *u-v* plane (Vogel et al. 1984) or at various stages in the image plane (Wong & Blitz 2002; Regan et al. 2001; Stanimirovic et al. 1999; Sault et al. 1996). In general, we found that for our sample, the best method to combine the maps was to use a method described in Stanimirovic et al. (1999), Regan et al. (2001), and Helfer et al. (2003). In this method, a new dirty map was created by combining the dirty interferometer map with the single-dish map. The primary beam response for the interferometer mosaic was not fully corrected so as to limit the noise amplification at the edges of the mosaic, where the sensitivity is low (Sault et al. 1996). This provides roughly uniform noise, to within a factor of a few, across the mosaic. The corresponding primary beam taper was applied to the single-dish maps. In the combining procedure, the interferometer and single-dish maps are weighted inversely proportional to the ratio of the beam areas and then added. A new dirty beam was also created by adding the BIMA synthesized beam and the 12 m beam, after applying the same weights. The new combined dirty map was then deconvolved using the Steer-Dewdney-Ito (Steer et al. 1984) clean algorithm. Table 4 lists the combined map parameters. The noise per channel (col. [5]) was measured off-source. The last three columns list the flux measured in the BIMA maps, NRAO 12 m maps, and the combined maps, respectively.

3. BIMA SAMPLE RESULTS

Our sample of eight evolved stars was selected from our larger study of *Infrared Space Observatory* (*ISO*) far-IR atomic fine-structure lines in the circumstellar envelopes of evolved stars

TABLE 4
Properties of the Combined Maps

Source (1)	Beam Size (arcsec) (2)	P.A. (deg) (3)	Channel Width (km s^{-1}) (4)	rms per Channel (Jy $beam^{-1}$) (5)	BIMA (Jy km s^{-1}) (6)	12 m (Jy km s^{-1}) (7)	Combine (Jy km s^{-1}) (8)
IRC +10216	13 × 12.9	63.2	2	0.4	3000	30000	30000
Mira	7.9 × 6.8	15.7	1	0.50	180	180	. . .
IRAS 22272+5435	4.0 × 3.6	7.0	1	0.21	200	200	. . .
HD 179821	3.4 × 2.9	20.4	4	0.17	520	400[a]	. . .
AFGL 2688	3.1 × 2.7	22.8	2.8	0.14	1200	2300	2300
HD 161796	3.8 × 3.4	54.1	2	0.11	80	80	. . .
89 Her	5.0 × 4.5	−8.5	1.5	0.08	50	. . .	. . .
NGC 7027	6.7 × 6.4	48.8	2	0.17	2300	2900	2900

[a] Observing conditions were poor during the observations, so the IRAM 30 m measurements (Bujarrabal et al. 1992) are stated in lieu of the NRAO 12 m measurements.

TABLE 5

Derived Parameters from the Combined Datacubes

Source	V_{LSR} (km s^{-1})	V_{exp} HWZP (km s^{-1})	Radius[a] (arcsec)	Inner Radius[b] (arcsec)	Deconvolved Size[c] (arcsec)	P.A.[c] (deg)	Peak Off[c] (R.A., Decl.) (arcsec)
IRC +10216	−26.0	14	190	...	130 × 127	40	2, 2
Mira	+46.7	−6/+4[d]	26	...	21.2 × 15.6	−42.6	0, 0
IRAS 22272+5435	−27.8	9	14	<1.9	8.1 × 7.5	60.4	0.5, −0.5
HD 179821	+98.5	37	10	1.6	...	...	1, 0
AFGL 2688	−35.0	−40/+35[d]	20.5	<1.5	11.4 × 10.6	26.0	−1, 0
HD 161796	−35.0	13	8.5	<1.8	4.4 × 3.9	−38.4	0.5, 1
89 Her	−8.2	8	12.5	DS[e]	9.7 × 9.5	−73.2	1.5, 1.5
NGC 7027	+26.0	22	40	5.5	33.6 × 33.1	−78.1	−0.5, 1

[a] Radial extent determined from an azimuthally averaged radial profile down to the zero level.
[b] Inner radius defined to be the half-intensity point between the intensity at the core and the peak intensity of the rim (for the azimuthally averaged radial profile at the systemic velocity channel). Upper limits are given for unresolved detached shells.
[c] The deconvolved size (FWHM), P.A., and peak offset were determined by 2D elliptical Gaussian fits to the systemic velocity channel.
[d] Double−shell structure.
[e] Asymmetric blueshifted/redshifted expansion velocities.

(Fong et al. 2001; Castro-Carrizo et al. 2001a). The sources selected also had known single-dish CO line detections, and some had been mapped with either single dish or interferometry, however, not with a full synthesis or mosaicked field interferometry strategy necessary to obtain the entire molecular envelope over scale sizes of 1″–400″. Our CO emission mapping of the sources investigates the evolution of the molecular gas by studying the size, morphology, and kinematics of the CO emission of some individual sources. Here we describe the results of the individual sources in the context of their evolutionary stage, AGB, PPN, and PN, comparing and contrasting the sources in these categories. In Table 5 the derived parameters from the combined spatial velocity datacubes are listed. Channel maps, line profiles, and position-velocity (PV) diagrams are presented for each source. For the PPNe and PN, comparisons with optical, near-IR, and mid-IR images that trace different regions of the CSE are shown.

3.1. *AGB Stars*

The AGB star stage is characterized by the intensive molecular winds that create the circumstellar envelope that eventually evolves into a PN. The wind velocities are expected to be slow, $\sim$10 km s^{-1}. The morphology of the envelopes is expected to be spherical based on the large study by Neri et al. (1998). The outer edge of the molecular gas is limited by photodissociation from the interstellar radiation field (ISRF). The inner regions are marked by strong IR emission from the circumstellar dust that is formed in the AGB wind, but we do not expect any photodissociation or ionized component of gas in the inner regions of the molecular envelope. In our sample, IRC +10216 is an archetype of an AGB star displaying many of these typical properties. In contrast, Mira appears to have a peculiar envelope that deviates significantly from expectations.

3.1.1. *IRC +10216*

IRC +10216 is a long-period variable with a period of about 650 days (Olofsson et al. 1982). At a distance of $\sim$150 pc (Groenewegen et al. 1998), it is one of the closest C-rich AGB stars with a high mass-loss rate. There have been numerous morphological studies of the circumstellar envelope. At subarcsecond scales, the dust shell was found to be very clumpy and generally bipolar in shape along an axis at P.A. = 10°–20° (e.g., Weigelt et al. 1998). Within the central 10″, *HST* images show a bipolar reflection nebula with a dark band separating the lobes (Skinner et al. 1998; Mauron & Huggins 2000). Recent deep *B*- and *V*-band images of the envelope show that on larger scales the star is surrounded by an extensive ($\sim$200″ radius) dust envelope composed of a series of multiple shell structures (Mauron & Huggins 1999, 2000). Groenewegen & Ludwig (1998) detected peculiar CO spectra with spikes that vary in strength with position around the envelope, which they interpret as a complex geometric structure. Here we present maps of the extended envelope of IRC +10216.

The velocity channel maps (Fig. 1) show that the global morphology of IRC +10216 is consistent with a spherically expanding envelope with a constant outflow velocity. This is evident in the channel maps where the systemic velocity component contains the most extended emission, while the increasingly blueshifted and redshifted velocities decrease in spatial extent until the most compact emission is seen at the extreme velocity caps situated at the center of the source. In addition, the parabolic line profile and the oval-shaped PV diagram with no velocity gradients are characteristic of a spherically expanding envelope.

CO emission is detected out to about 190″ from the central star, determined from the azimuthally averaged radial intensity profile. The outer extent is comparable to the size measured from CO strip maps (Huggins et al. 1988). The low surface brightness outer envelope is very broad and gradually increases in brightness toward the center. A striking feature about the outer envelope is the arc structures superposed on the smooth envelope emission. The full description of these molecular arcs is presented in Fong et al. (2003). The intensity of the CO emission increases dramatically within the inner 40″ radius, with the brightest emission concentrated at the core. The core features a subtle N-S elongation, roughly aligned with the optical bipolar axis. This N-S protrusion is most noticeable out to 40″ in radius. The bright, central CO emission is comparable to the distribution of HCN and $H^{13}CN$ mapped by Dayal & Bieging (1995). The HCN and $H^{13}CN$ maps are concentrated at the core and also exhibit a slight, north-south elongation.

3.1.2. *Mira*

Mira is the prototype long-period Mira variable, with a brightness variation of 7 mag over a period of 332 days (Karovska et al. 1997). It is one of the closest O-rich AGB stars at a distance of 128 pc (*Hipparcos* Catalog). Mira forms a binary system with a white dwarf companion, separated by an angular distance of about 0.″6 at a position angle (P.A.) of 108° (Karovska et al. 1997). The

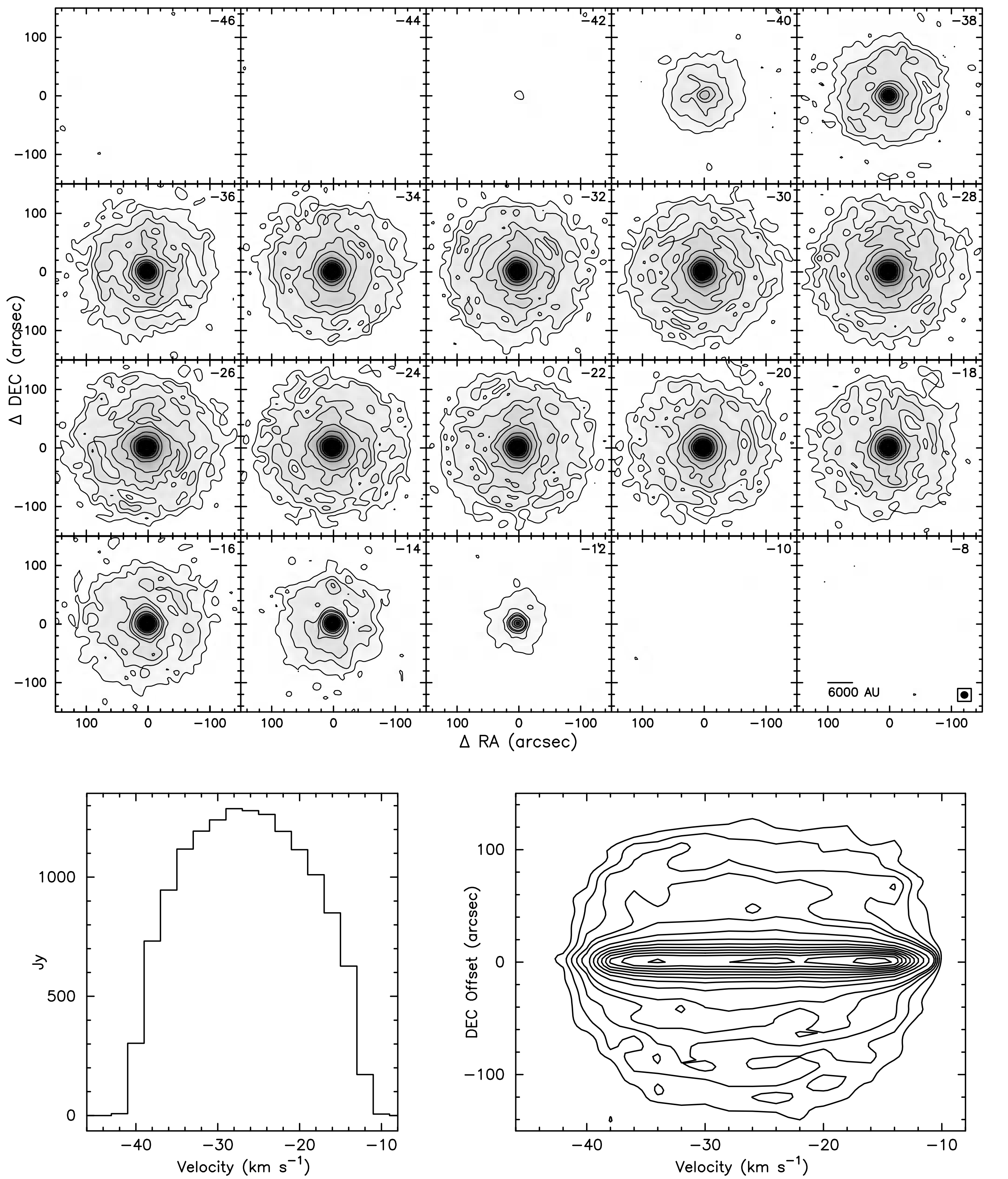

FIG. 1.—IRC +10216. *Top*: Channel maps with 2 km s^{-1} widths. The first five contours levels are in increments of 3.5 σ ($\sigma = 0.4$ Jy beam^{-1}), and the remaining contours are in levels of 10.5 σ. The beam is shown in the −8 km s^{-1} channel. *Bottom left*: CO line profile. *Bottom right*: PV diagram cut along P.A. = 0°, with similar contours as above.

orbital plane of the Mira A/B system is nearly edge-on with an orbital inclination of 111° (Reimers & Cassatella 1985). Previous molecular observations revealed a spherical envelope with north-south bipolar outflows (Planesas et al. 1990a, 1990b). However, their ^{12}CO $J = 1 \rightarrow 0$ interferometer maps were missing 80% of the flux from the extended structures. Here we present CO maps that contain all of the flux with comparable resolution (Fig. 2).

The morphology of Mira is distinctly nonspherical (Fig. 2). The bright emission at 47 km s^{-1} is extended along several protrusions. The core region contains an east-southeast–west-northwest bulge and also protrudes toward the south. In the outer envelope, the longest protrusion is found along the northeast-southwest direction. This northeast-southwest bar has an extent of almost 60″. Just northwest of this bar lies a pinched waist along the same P.A. and in line with the position of the central star. Above this pinched waist, along the same angle, are hints of another northeast-southwest bar. The general morphology of the emission is not round, but flattened along the top and bottom edges, parallel to the bar. Similar features are found in adjacent velocity channels. At 48 km s^{-1}, two bars with a pinched waist in between are present, along with a north-south protrusion stemming from the core region. The bar feature is also seen in the remaining redshifted channels and in the two adjacent blueshifted channels. At 45 km s^{-1}, two bars are evident with depressed emission in between. At 44 km s^{-1}, the bars are no longer apparent and a possible self-absorption feature is present. These northeast-southwest structures are also noticeable in the high-resolution CO $J = 1 \rightarrow 0$ (Planesas et al. 1990b) and $J = 2 \rightarrow 1$ (Josselin et al. 2000) images. The protrusions in the molecular envelope may have their origins from tidal interactions or wind interactions with the companion.

The kinematics of Mira reveals more than simple expansion. A striking feature about the kinematics of Mira is the small expansion velocity (Fig. 2). The emission peaks at the systemic velocity (46.7 km s^{-1}) and the redshifted wing extends 4 km s^{-1}, while the blueshifted wing extends 6 km s^{-1}. The shape and position of the main CO emission bulge change with velocity. At 46 km s^{-1}, the emission is approximately centered near the central star position. At redshifted velocities, the emission extends southeast of the star with the large extension at 47 km s^{-1}. This southeast extension decreases in size with increasing (i.e., more redshifted) velocity until the CO emission is compact and centered on the star again at 50 km s^{-1}. At blueshifted velocities, the emission extends to the northwest with the largest extension at 45 km s^{-1}. This northwest extension decreases in size with the decreasing (i.e., more blueshifted) velocity until the CO emission is compact and centered again at 41 km s^{-1}. Mira's peculiar velocity structure was modeled with three velocity components arising from the circumstellar envelope expansion and a bipolar outflow by Planesas et al. (1990a, 1990b) and Josselin et al. (2000). We propose that disk rotation may be a more plausible alternative interpretation of this structure. This morphological change of CO emission with velocity shows some similarities to recent observations of gravitationally bound gas in the post-AGB source, the Red Rectangle (e.g., Bujarrabal et al. 2003, 2005). Supporting this disk rotation interpretation, the axis aligning the redshifted and blueshifted elongated structures is roughly aligned with the edge-on orbital plane of the Mira A/B system at a P.A. of 108° (Karovska et al. 1997; Reimers & Cassatella 1985). The PV diagram, which is taken along a 0° cut, possibly shows a combination of expansion and rotation.

3.2. *PPNe*

PPNe have many of the features of AGB stars, but the circumstellar shells are expected to be detached because the AGB mass-loss phase has ended. Optical reflection nebulae and IR thermal emission from the dust shell may represent the inner structures not resolved by our molecular images. We do not expect ionized gas, but low-excitation atomic emission or near-IR H_2 emission from emerging photodissociation regions (PDRs) and shocked gas regions may be present. Slow or fast molecular winds, possibly in collimated structures, may be common in most PPNe (Bujarrabal et al. 2001), but we expect no fast ionized wind because the star is too cool to have a line-driven wind. Here we describe five PPN candidates. AFGL 2688, aka the Egg Nebula, is an archetype of the PPN class having many of the most complex features observed in DUPLEX PPNe. In contrast, the PPNe IRAS 22272+ 5435 and HD 161796 show the more simple features of SOLE PPNe. The PPN 89 Her has not been classified as either a SOLE or DUPLEX PPN, and our observations may suggest that it is in an entirely different class. HD 179821, often classified as a PPN candidate and classified as a SOLE nebula by Ueta et al. (2000), is most likely a yellow hypergiant.

3.2.1. *AFGL 2688*

The PPN AFGL 2688 is the most well-known object in transition from the AGB to the PN phase. Optical to millimeter-wave observations have shown that it hosts a number of transitional structures such as a roughly spherical molecular envelope, concentric dust arcs, optical bipolar lobes separated by a dark band across the waist, and quadrupolar H_2 emission features (e.g., Truong-Bach et al. 1990; Kawabe et al. 1987; Ney et al. 1975; Latter et al. 1993; Sahai et al. 1998a, 1998b). High-resolution ^{12}CO $J = 2 \rightarrow 1$ observations have revealed a series of collimated bipolar outflows, where the main CO outflows correspond to the quadrupolar H_2 emission seen in *HST* images (Cox et al. 2000). Although their CO observations achieve a resolution that is 3 times better than our maps, their images show only the bright structures within the inner 7″ in radius and are missing substantial flux associated with more extended emission.

The CO $J = 1 \rightarrow 0$ velocity channel maps (Fig. 3) reveal the morphology and kinematics of multiple wind components. The first component is the slow AGB wind that ranges from about −50 to −22 km s^{-1}. The AGB envelope is slightly elliptical and extends about 28″ north-south and 22″ east-west at the 2 σ level. Superposed within this extended AGB wind lies the high-velocity outflow components. At the systemic velocity (−36 km s^{-1}), there are signs of quadrupolar structures protruding nearly north-south and east-west from the inner 9″ in radius. Stepping to more redshifted velocities, a "boomerang"-type structure gradually appears more distinct from the AGB envelope, until it emerges from the AGB wind beyond −22 km s^{-1}. The nearly north-south part of this feature is oriented along the optical bipolar axis, while the nearly east-west feature is close to the equatorial plane. A similar structure is seen at blueshifted velocities, but the boomerang is transposed north-south and east-west. Between −56 and −50 km s^{-1}, the blueshifted emission is self-absorbed. This absorption feature is clearly evident in the line profiles (Fig. 4). The spectra also show the parabolic profile of the expanding AGB wind and high-velocity wings.

The high-velocity winds can be decomposed into two bipolar outflows: one along the optical axis and the other along the equatorial plane. The PV diagrams (Fig. 4) along these two axes show the kinematics more clearly. At P.A. = 14° the bipolar outflow is seen as the velocity gradient starting at the extreme blueshifted velocities with small positive position offsets and ending at the extreme redshifted velocities at small negative position offsets. The extended emission from about −50 to −20 km s^{-1} is the AGB component. The bipolar outflow along the equatorial plane

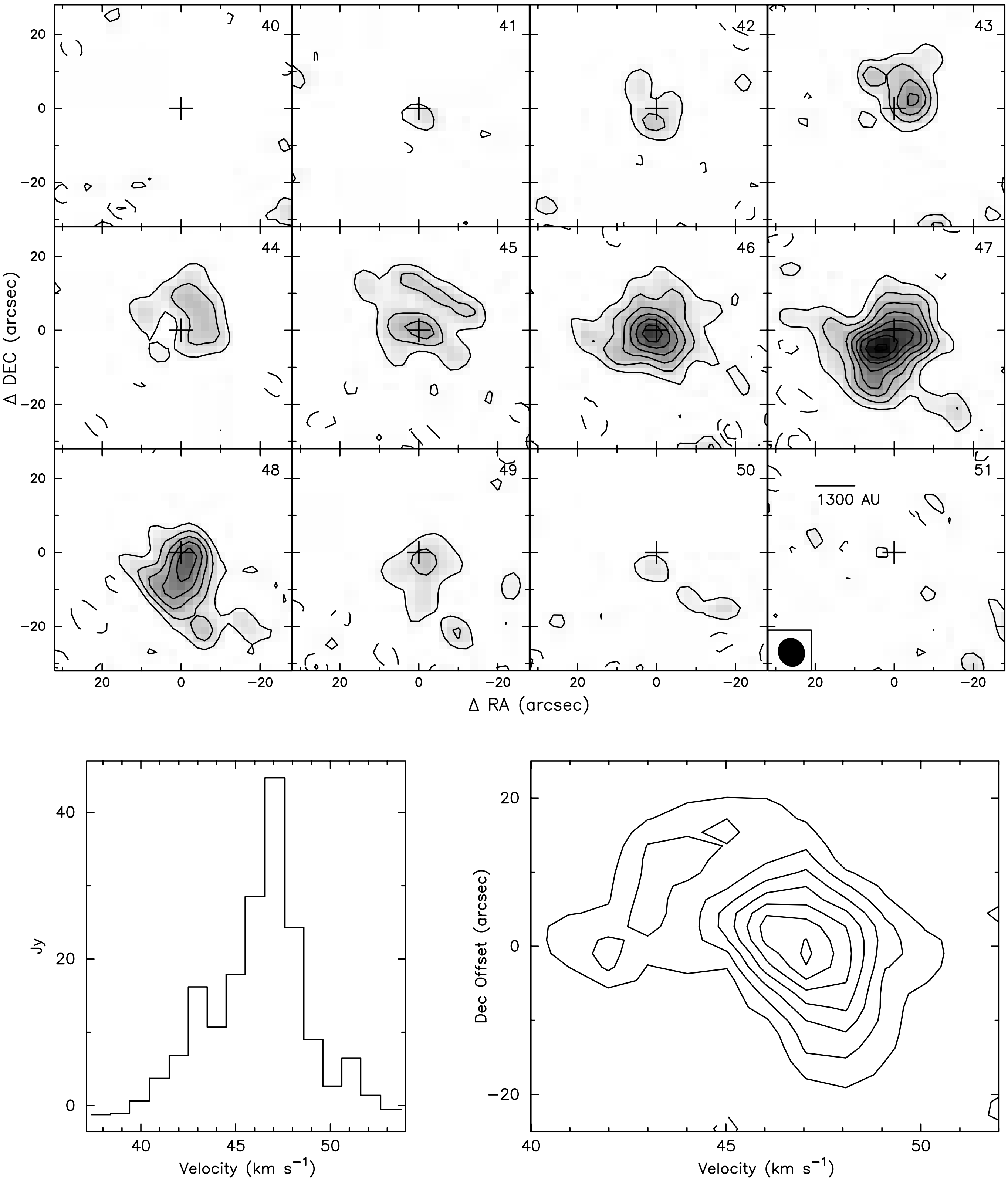

FIG. 2.—Mira. *Top*: Channel maps with 1 km s^{-1} widths; the contour levels are in increments of 2 σ ($\sigma = 0.5$ Jy $beam^{-1}$). *Bottom left*: CO line profile. *Bottom right*: PV diagram cut along P.A. $= 0°$, with similar contours as above.

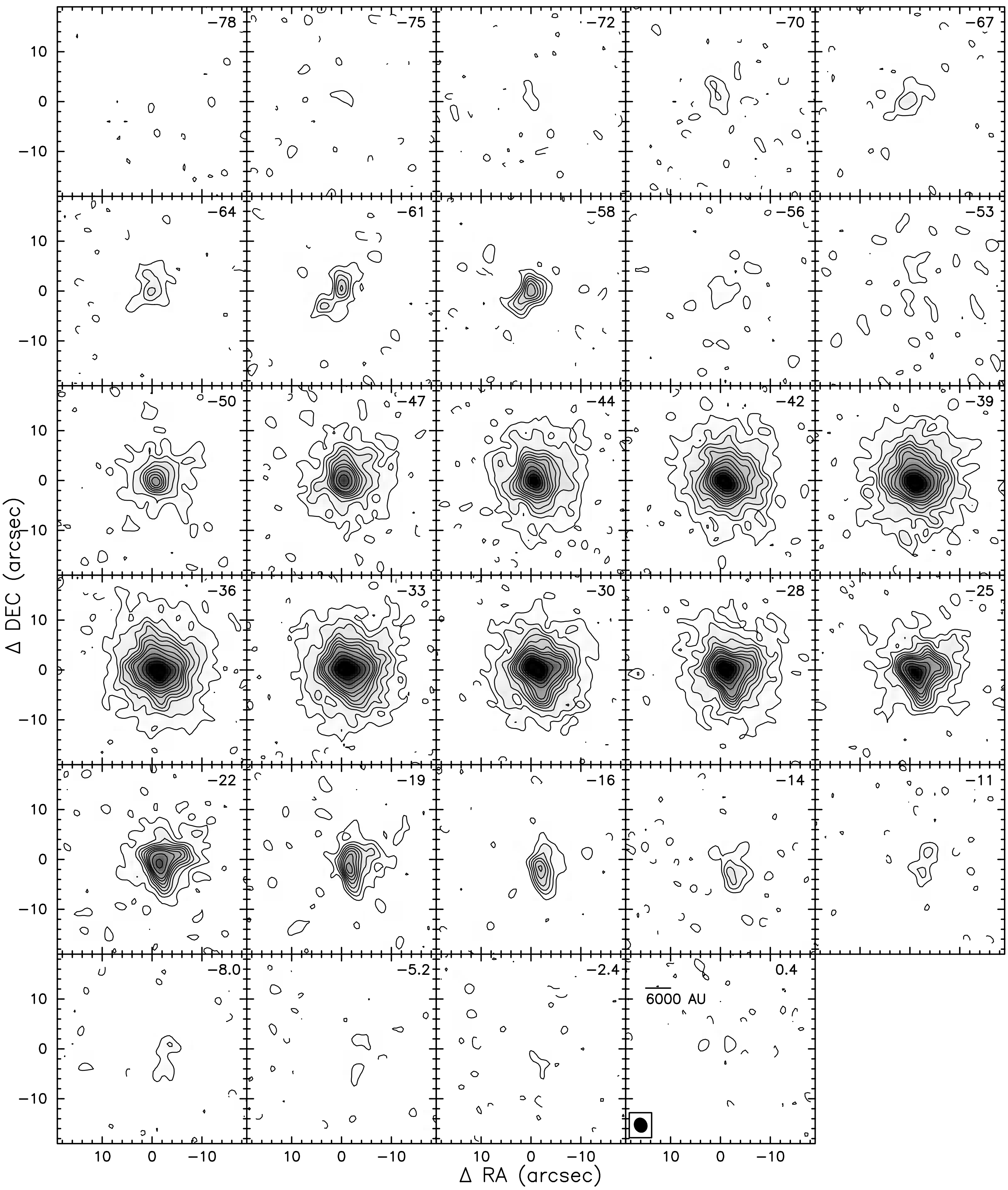

FIG. 3.—Channel maps with 4 km s^{-1} widths for AFGL 2688. The first eight contour levels are in increments of 2 σ ($\sigma = 0.14$ Jy $beam^{-1}$), and the remaining contours are in levels of 4 σ.

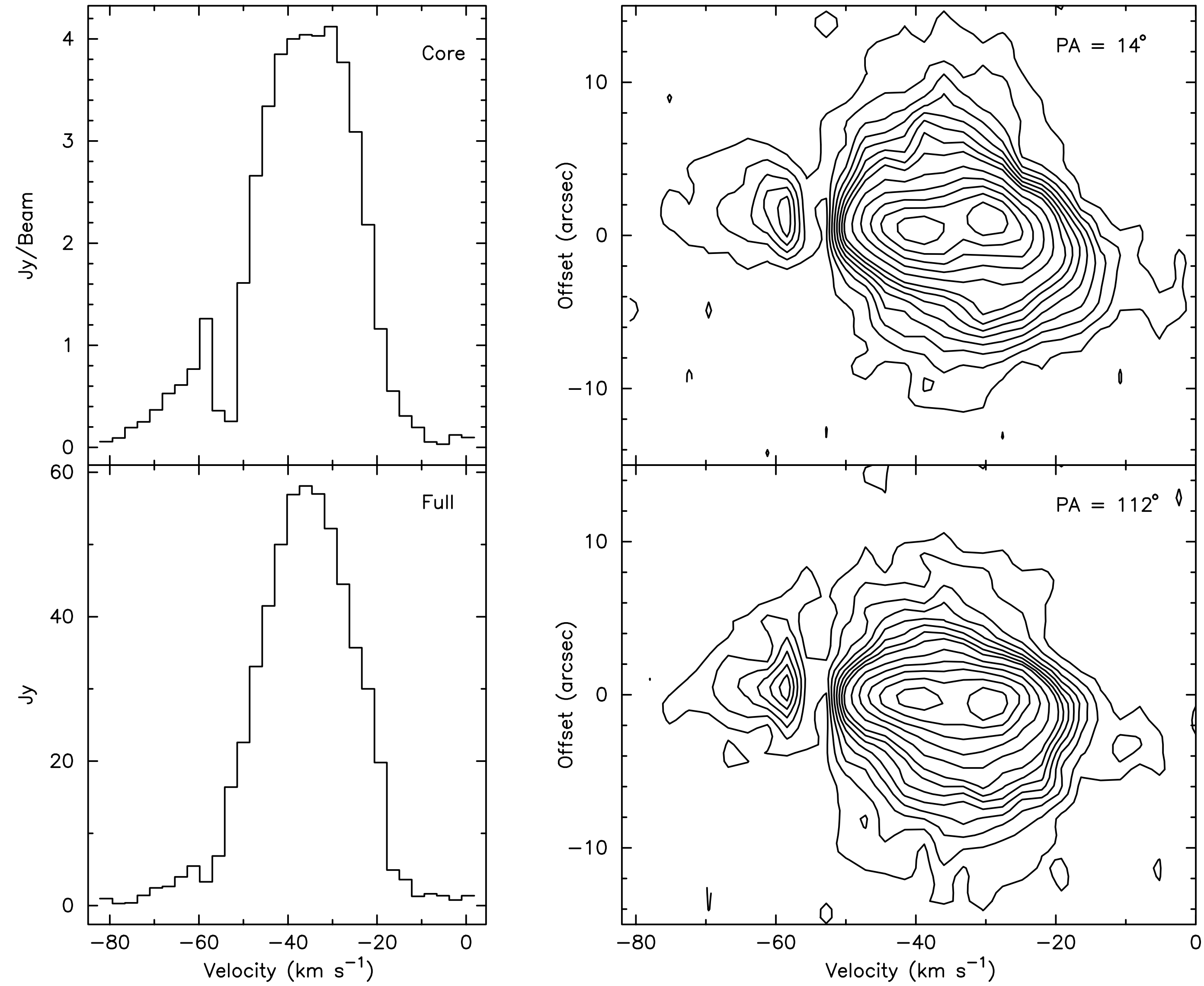

FIG. 4.—AFGL 2688. *Left*: Line profile of the central core (central 5″) emission region and of the full envelope. *Right*: PV diagram cut along the optical bipolar axis (P.A. = 14°) and along the equatorial waist (P.A. = 112°). The contour levels are similar to the channel maps.

shows similar features in the PV diagram at P.A. = 112°. The high-velocity outflows are present at small position offsets, which suggests that these fast structures have emerged relatively recently from the core.

The overlay image (Fig. 5, *top left*) shows the high-velocity blueshifted (≤ -57 km s^{-1}) and redshifted (≥ -19 km s^{-1}) emission in the blue and red contours, respectively. The position of the extreme blueshifted velocity structure is offset along the optical axis, from the extreme redshifted structure. The color background displays the velocity-integrated image. At the interface where the high-velocity outflows interact with the slower AGB wind, shocked H_2 emission is detected as red in the color composite *HST* image (Fig. 5, *top right*). This provides clear evidence of AGB and post-AGB wind interaction and its process in shaping the nebula.

3.2.2. *IRAS 22272+5435*

IRAS 22272+5435 is a C-rich PPN with a G5 Ia central star. It has been discovered to have strong IR features at 21 μm (Kwok et al. 1989) and 30 μm (Omont et al. 1995). Morphological investigations of IRAS 22272+5435 have been conducted at optical (Ueta et al. 2000), near-IR (Gledhill et al. 2001a), and mid-IR wavelengths (Meixner et al. 1997; Ueta et al. 2001b). These studies have found a symmetry axis at P.A. $\sim -35°$, suggested by the optical and near-IR elongation and a toroidal dust shell along the perpendicular direction. Here we present CO maps with high enough resolutions to show features comparable to those in the optical and mid-IR images.

The velocity channel maps are displayed in Figure 6. The morphology and kinematics of the molecular gas are roughly consistent with a spherically expanding envelope. On smaller scales, the envelope clearly deviates from spherical symmetry. The deviations are better described as multiple protrusions found in the envelope. The morphology at -26 km s^{-1} highlights these features, where four protrusions are found in an X-shaped geometry. This quadrupolar geometry extends farther into the envelope, giving the core region an almost squarelike appearance. Other disturbances are also present, particularly to the north-south, but these features are present only along the outer contours and do not extend farther inward. This quadrupolar shape is generally seen in the other velocity channels but does not appear as pronounced. The parabolic line profile with an expansion velocity of 9 km s^{-1} is

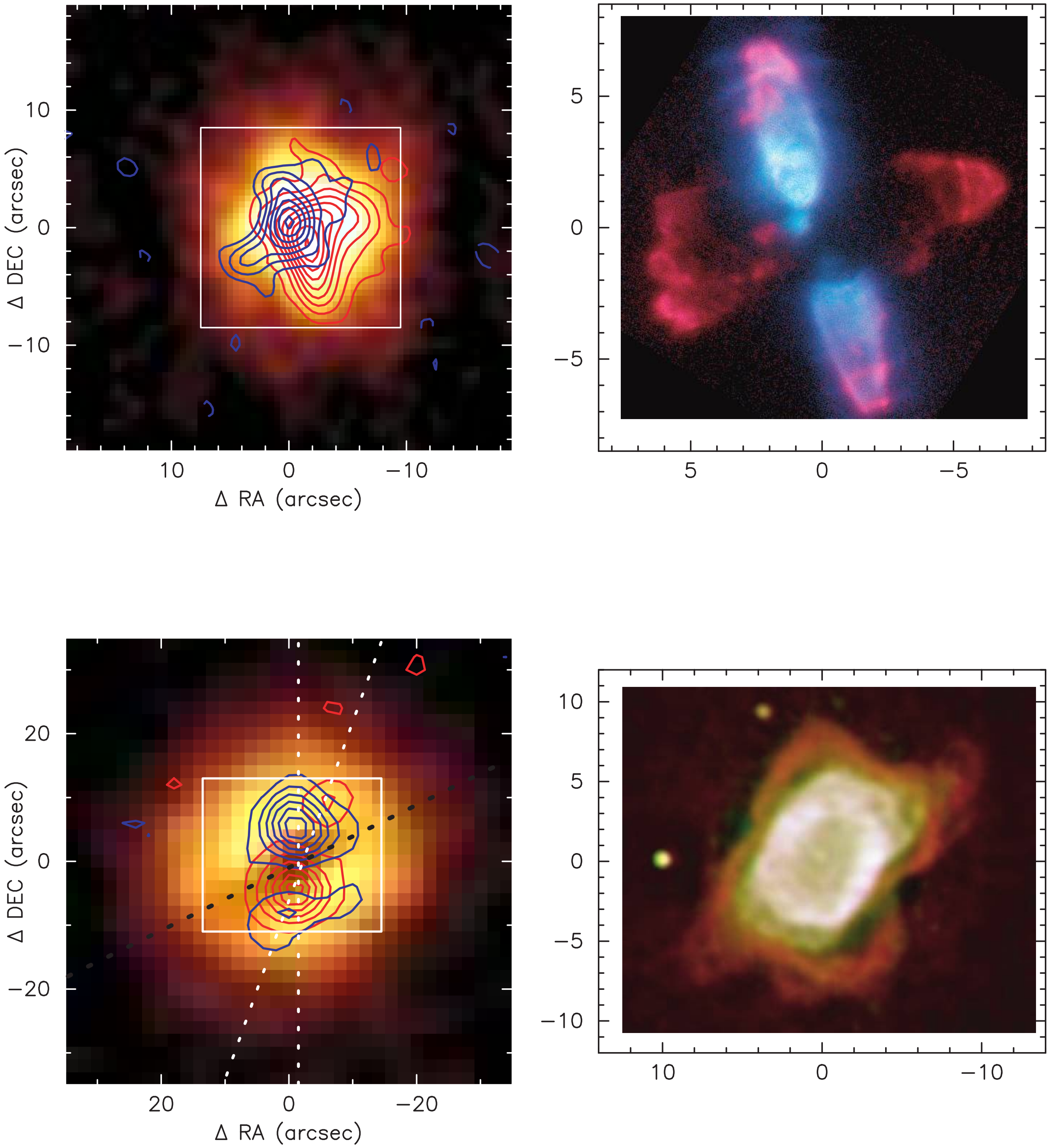

FIG. 5.—*Top*: AFGL 2688; *bottom*: NGC 7027. *Top left*: High-velocity blueshifted and redshifted outflows in blue and red contours overlaid on the color background of the velocity-integrated map. The white box corresponds to the region shown on the right. *Top right*: Color composite *HST* image (adapted from Thompson et al. 1997) with H_2 in red and scattered starlight in blue. *Bottom left*: High-velocity blueshifted and redshifted outflows in blue and red contours overlaid on the color background of the systemic velocity map. The white box corresponds to the region shown on the right. *Bottom right*: Color composite image of NGC 7027 taken using NIRIM at WIYN, with the vibrationally excited H_2 in red, [Fe II] in yellow, and Brγ in blue.

typical of a C-rich expanding envelope (Loup et al. 1993). The PV diagram does not show any evidence for outflow structures that can give rise to the quadrupolar morphology in the molecular envelope.

A morphological comparison between the CO map at -26 km s^{-1} and the optical and mid-IR images is shown in Figure 7. The top right panel shows the *V*-band *HST* image overlaid with contours of the deconvolved 11.7 μm MMT map (from Ueta et al. 2001b). The optical image shows a central star with a faint quadrupolar nebulosity in dust-scattered starlight, while the mid-IR image directly traces the warm dust distribution. The directions of three optical protrusions toward the north, west, and

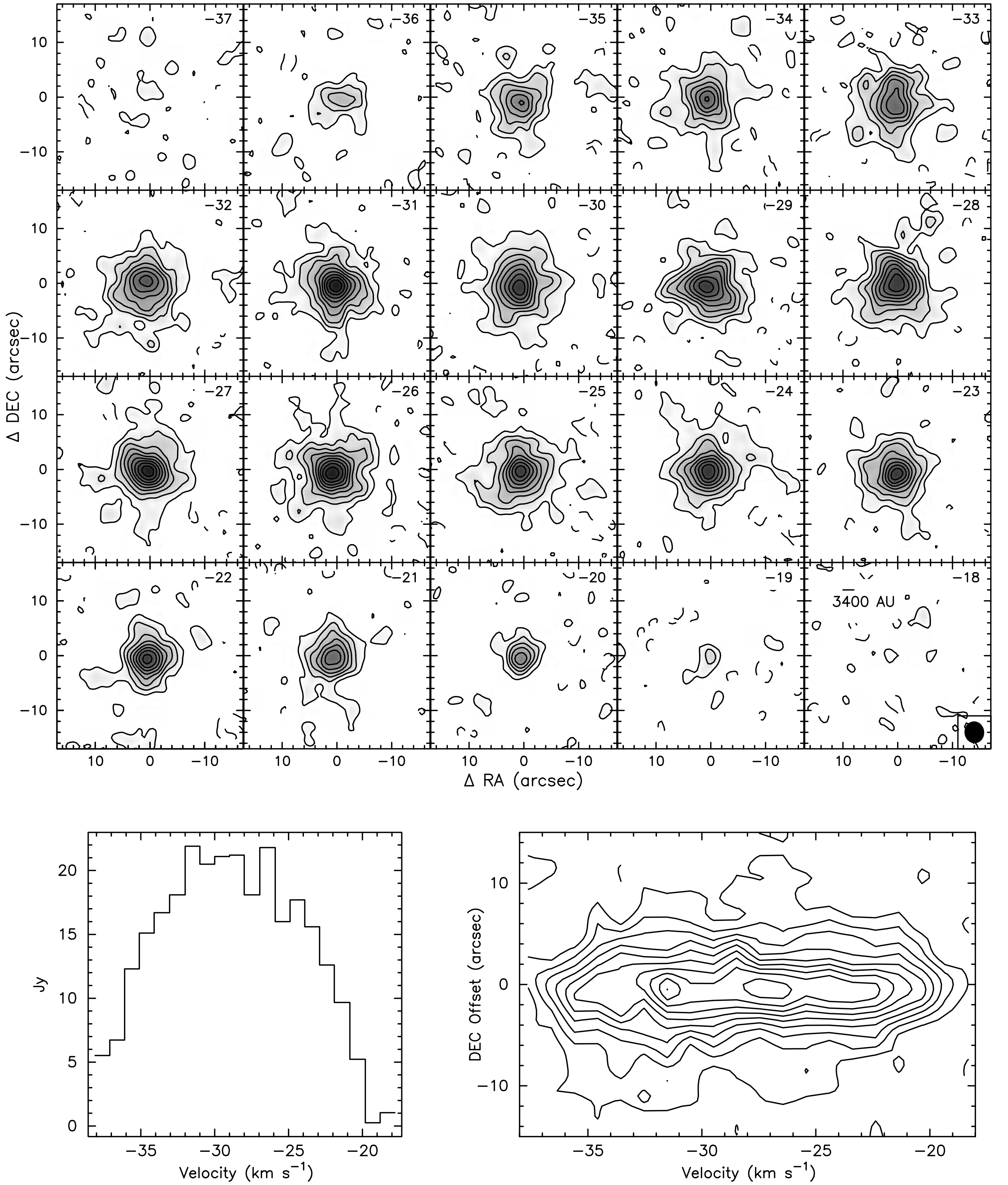

FIG. 6.—IRAS 22272+5435. *Top*: Channel maps with 1 km s^{-1} widths; the contour levels are in increments of 2 σ ($\sigma = 0.21$ Jy beam^{-1}). *Bottom left*: CO line profile. *Bottom right*: PV diagram cut along P.A. $= 0^{\circ}$, with similar contours as above.

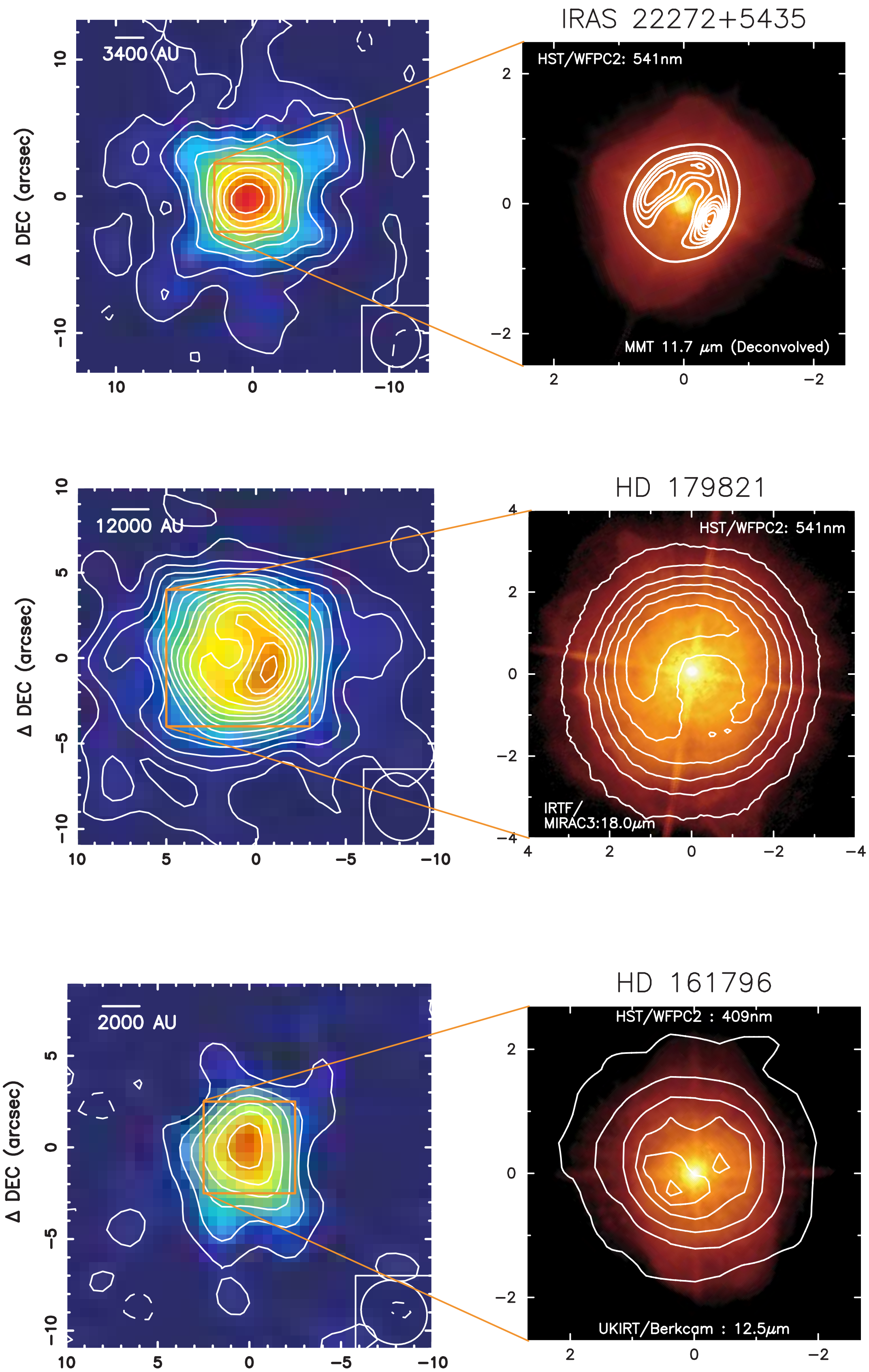

FIG. 7.— *Top left*: IRAS 22272+5435 CO channel map at -26 km s^{-1}. *Middle left*: HD 179821 CO intensity map integrated over 79–115 km s^{-1}. *Bottom left*: HD 161796 CO channel map at -32 km s^{-1}. *Right panels*: Corresponding optical images overlaid with mid-IR contours for IRAS 22272+5435 (Ueta et al. 2001a), HD 179821 (Ueta et al. 2000), and HD 161796 (Meixner et al. 2002).

south-southeast are coincident with openings/depressions in the mid-IR dust distribution. The CO map appears to trace out the optical quadrupolar structure but on a larger scale, with three CO protrusions roughly aligned with three of the optical lobes. Although the northern optical lobe does not appear to have an associated CO protrusion at this velocity channel, other velocity channels (e.g., -25 km s^{-1}) do show a northern protrusion. Molecular features corresponding to the toroidal dust shell were not detected because it is unresolved. Ueta et al. (2001b) interpret the large break in the dust distribution toward the south-southeast as a blowout; however, the gas kinematics does not support this or other outflows that could have created this unusual quadrupolar structure. Additional evidence is provided by far-IR line observations, where nondetections of atomic fine-structure lines imply that the molecular envelope has not been transformed by shocks or photodissociation.

3.2.3. *HD 161796*

HD 161796 is a high Galactic latitude F2–F5 supergiant (Hrivnak et al. 1989), with low-amplitude variability ($\sim$0.1–0.2 mag) over a period of 41 days (Fernie & Seager 1995). OH maser emission (Likkel 1989) and silicate dust features (Justtanont et al. 1992) confirmed the O-rich circumstellar environment around this PPN. Morphological investigations of HD 161796 have been conducted at optical (e.g., Ueta et al. 2000) and mid-IR wavelengths (Skinner et al. 1994; Meixner et al. 1999b). These studies have found a north-northeast–south-southwest symmetry axis and evidence for a toroidal dust shell along the perpendicular direction (Meixner et al. 2002). Here we present high-resolution maps of the molecular envelope surrounding these optical and mid-IR features.

The velocity channel maps are shown in Figure 8. The spatial distribution and kinematics of the molecular gas are roughly consistent with a spherically expanding envelope. Although the morphology changes from channel to channel, the general shape appears slightly elliptical to the north-south, with protrusions in the outer envelope. A notable southern protrusion is found from -44 to -32 km s^{-1}. At some channels the protrusion extends from the inner region (e.g., at -42 km s^{-1}), while at other channels the southern protrusion is traced mainly in the outer 2 σ contour. Since this feature is coherent across a range of velocities, this suggests that the protrusion is real. The parabolic line profile with an expansion velocity of 13 km s^{-1} is typical of an expanding envelope of an O-rich PPN. The PV diagram does not show any evidence for an outflow structure that can give rise to the protrusions.

A morphological comparison between the CO map at -32 km s^{-1} and the optical and mid-IR images is shown in Figure 7. The right panel shows the *V*-band *HST* image overlaid with contours of the 12.5 μm UKIRT/Berkcam map (from Meixner et al. 2002). The optical image shows a central star with a faint elliptical nebulosity in dust-scattered starlight, while the mid-IR image shows limb-brightened edges of an optically thin dust torus. The CO map appears to trace out the elliptical nebulosity but on a larger scale. The presence of low-intensity wings in the ^{12}CO $J = 2 \rightarrow 1$ line has been suggested to correspond to high-velocity bipolar outflows by Bujarrabal et al. (1992). However, we do not detect gas outflows that may give rise to the elliptical structure.

3.2.4. *89 Her*

89 Her is a well-studied, low-luminosity PPN. Long-term monitoring of its visible light and velocity reveals a 63 day period arising from pulsations (Fernie 1981) and a 288.4 day period most likely caused by a low-mass ($>$0.073 $M_{\odot}$) binary companion with a velocity amplitude of 3 km s^{-1} (Waters et al. 1993). The circumstellar dust, as evidenced by an infrared excess, has been modeled as a double shell of dust emission with an inner shell of warm dust emission and an outer shell of cooler dust (Alcolea & Bujarrabal 1991). Mid-infrared images show that the warm dust emission is unresolved (Meixner et al. 1999b). Waters et al. (1993) suggested that the dust was distributed in a circumstellar disk where the line of sight toward the star does not intersect the disk because there was negligible extinction toward the central star. The recent finding of strong crystalline silicate dust features in 89 Her and other PPNe with circumstellar disks suggests that the creation of these crystalline silicates requires the long-term stability of a disk (Molster et al. 2002a, 2002b).

Molecular gas studies of 89 Her reveal a peculiar CO line profile with a narrow core of 2 km s^{-1} and broader wings of 8 km s^{-1} (Likkel et 1987; Bujarrabal et al. 2001). The distribution of molecular gas shows evidence for two shells as suggested by dust studies (Alcolea & Bujarrabal 1995). The CO maps that we present here have comparable resolution to those of Alcolea & Bujarrabal (1995), but our image quality is better due to the improved *uv* coverage. Our maps confirm their finding of a double-shell structure that is best seen in the channel maps (Fig. 9). The outer shell spans the entire velocity range of the broad wings seen in the line profile and shows characteristics of a clumpy shell expanding away from the central star. The channel maps at -11 and -4.9 km s^{-1} show evidence for a hollow center to this outer shell. The outer shell exhibits an asymmetry in the shell structure with more emission on the western half of the nebula. This is clearly seen in the PV diagram as the flared-out contour features at negative right ascension position offsets (Fig. 9). In addition, this bright western emission has a north-south elongation.

The inner shell is only present in the narrow velocity range of the line core, from -9.5 to -6.4 km s^{-1} in the channel maps. The inner shell fills in the hollow center of the outer shell in these velocity channels, giving the appearance of an unresolved circumstellar envelope in these channels. The inner shell appears marginally resolved by our beam. The channel maps of -9.5 and -8.0 km s^{-1} reveal a shift of $2''$ in the peak location of the CO line emission from west to east. This movement can also be seen in the PV diagram where the peak at -10 km s^{-1} is located at $-1''$ in right ascension offset and shifts to $+1''$ at -8 km s^{-1}. If we interpret the inner shell as the circumstellar disk suggested by Waters et al. (1993), then this shift may be associated with a disk rotation. Our resolution is not sufficient to separate the outer and inner shells, but a higher resolution map by Alcolea & Bujarrabal (1995), made with uniform *uv* data weighting, suggests that they are distinct. There does not appear to be any kinematic interaction between the inner disk and outer shell.

3.2.5. *HD 179821*

HD 179821 is of spectral type G5 Ia (Hrivnak et al. 1989). It is a well-studied O-rich object whose nature remains controversial because its distance is not well determined. For arguments favoring a post-AGB star at a distance of 1 kpc, refer to Josselin & Lèbre (2001), and for arguments suggesting a hypergiant star located at a distance of 6 kpc, see Jura et al. (2001). HD 179821 was previously imaged in the optical (Ueta et al. 2000), near-IR (Gledhill et al. 2001a), and mid-IR (Hawkins et al. 1995; Jura & Werner 1999; Ueta et al. 2001a). This object was also previously mapped in ^{12}CO $J = 1 \rightarrow 0$ using the Owens Valley Radio Observatory (OVRO; Jura et al. 2001), in ^{12}CO $J = 2 \rightarrow 1$ using IRAM 30 m (Bujarrabal et al. 1992), and the OH maser emission was mapped using MERLIN (Gledhill et al. 2001b). Near-IR to radio images show a detached shell structure with an inner radius

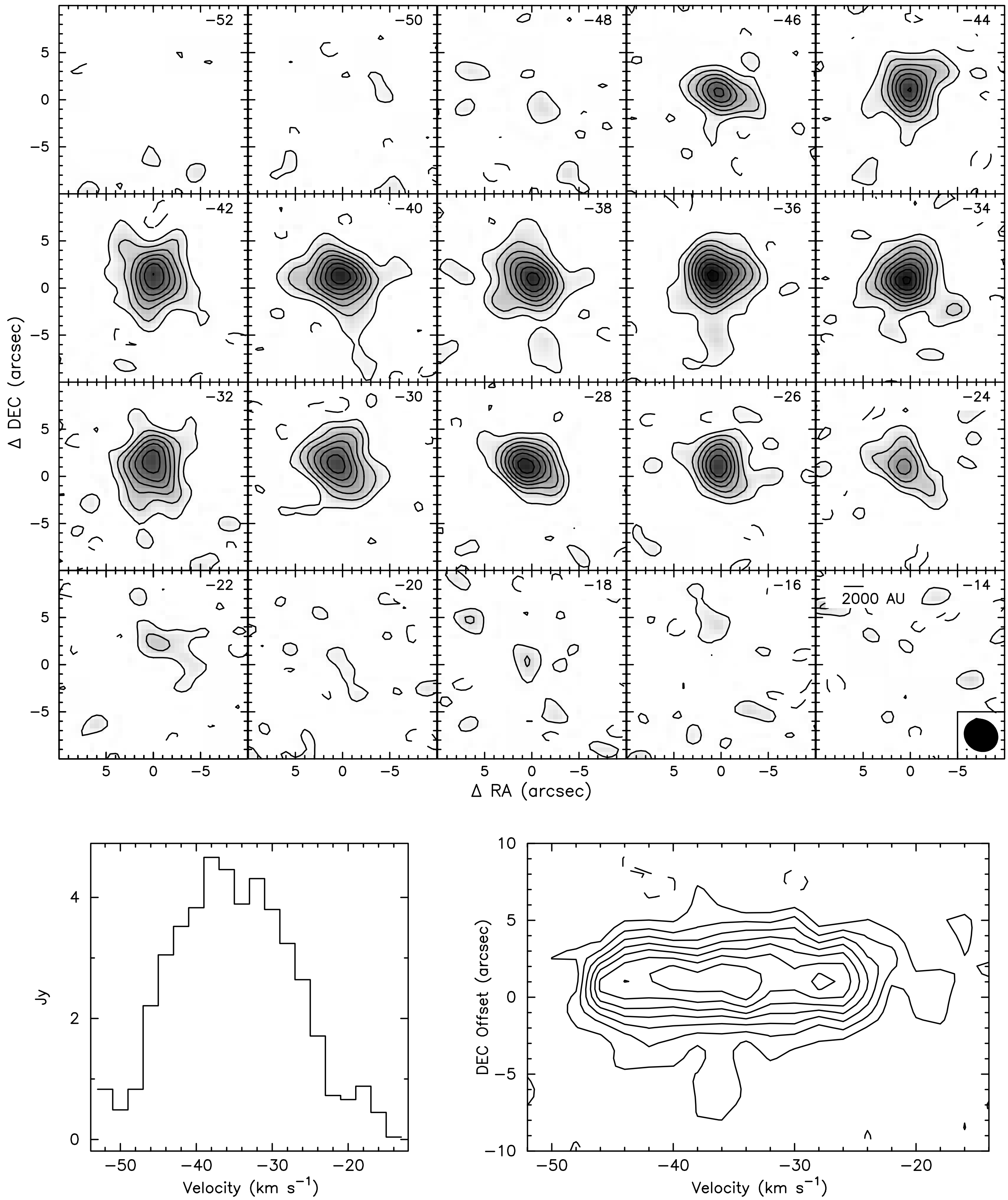

FIG. 8.—HD 161796. *Top*: Channel maps with 2 km s^{-1} widths; the contour levels are in increments of 2 σ ($\sigma = 0.11$ Jy beam^{-1}). *Bottom left*: CO line profile. *Bottom right*: PV diagram cut along P.A. = 0°, with similar contours as above.

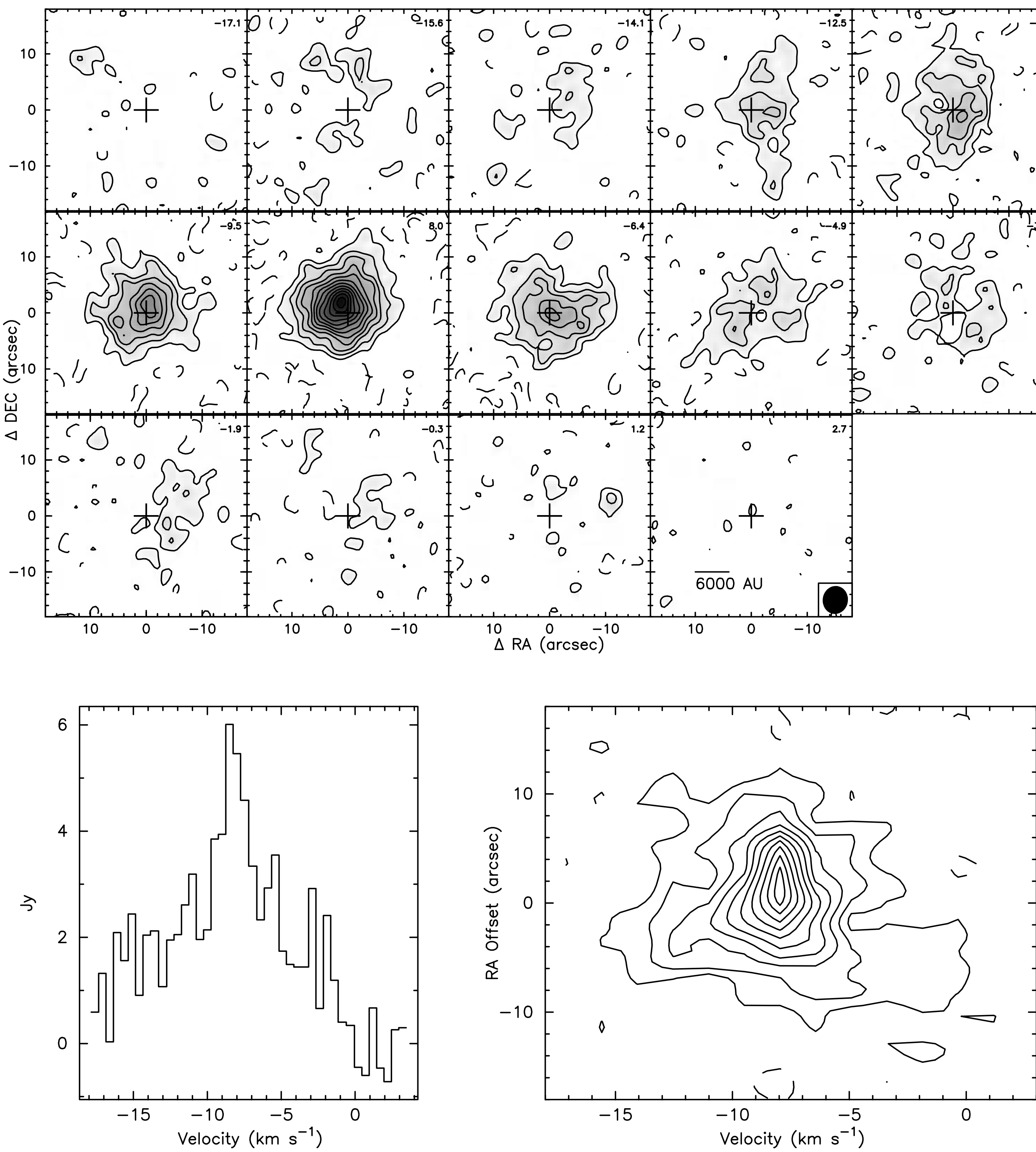

FIG. 9.—89 Her. *Top*: Channel maps with 1.5 km s^{-1} widths; the contour levels are in increments of 2 σ ($\sigma = 0.08$ Jy beam^{-1}). *Bottom left*: CO line profile. *Bottom right*: PV diagram cut along P.A. $= 90°$, with similar contours as above.

of about 2″. This shell structure is most likely caused by a cessation of mass loss with the ejected material just coasting outward. Far-IR spectral observations also show no detections of photodissociated or shock-induced emission such as [O I] 63 μm and [C II] 158 μm (Castro-Carrizo et al. 2001a).

The velocity channel maps with 4 km s^{-1} widths are shown in Figure 10. The morphology and kinematics of the gas are generally consistent with a spherically expanding shell with a constant outflow velocity of 37 km s^{-1}. The systemic velocity channel (99 km s^{-1}) shows a bright, clumpy ring of emission with a depressed central hole. This ring structure is generally seen at the intermediate expansion velocities, from 79 to 115 km s^{-1}, although the ring is very clumpy and the central hole is not obvious at certain velocity channels. The plus sign overlaid on each channel indicates the position of the central star. The central star is located within the central hole and not on the peak of the CO

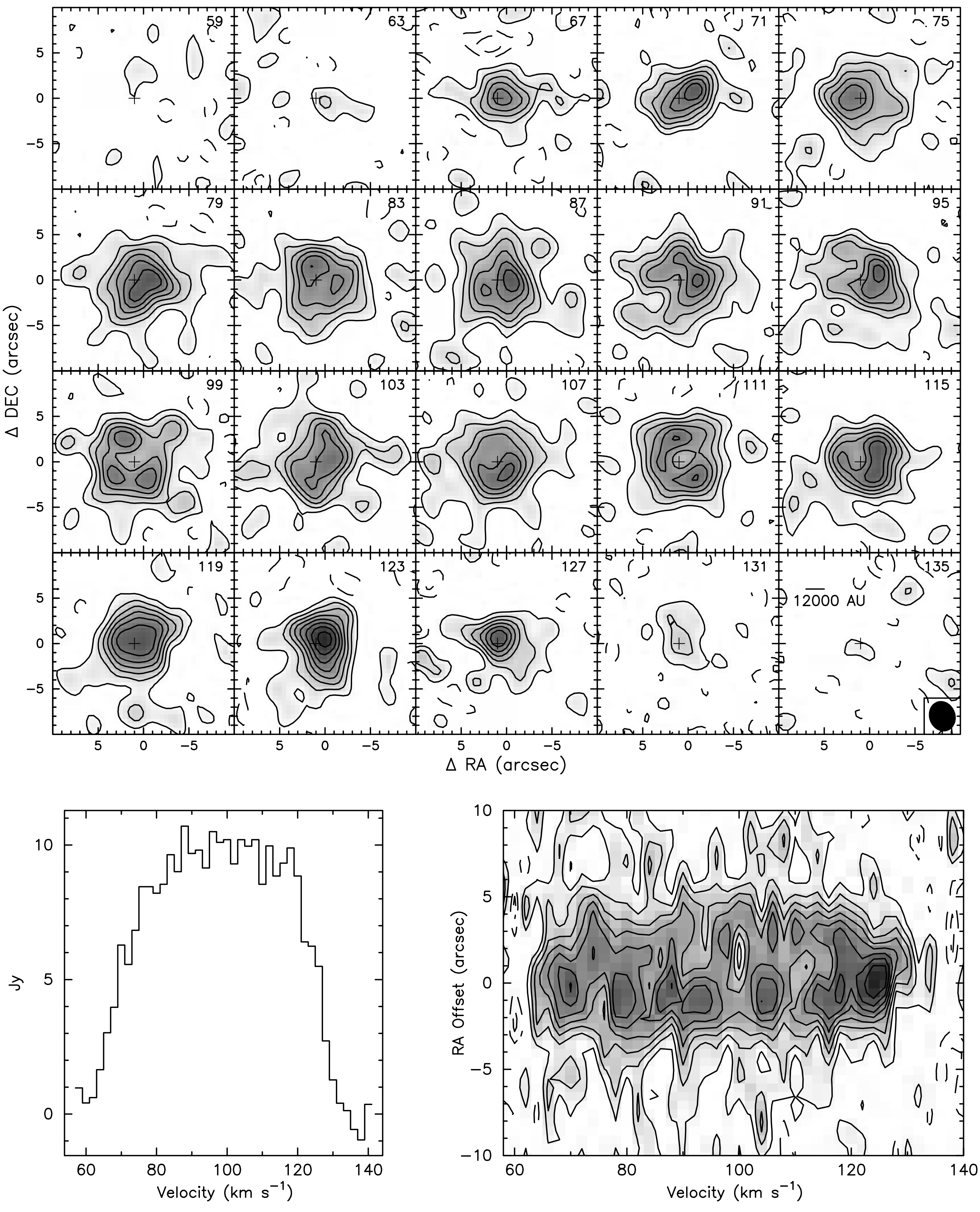

FIG. 10.—HD 179821. *Top*: Channel maps with 4 km s^{-1} widths; the contour levels are in increments of 1.5 σ ($\sigma = 0.17$ Jy beam^{-1}). *Bottom left*: CO line profile. *Bottom right*: PV diagram cut along P.A. = 90°, with similar contours as above.

emission. Our BIMA observations are generally similar to the OVRO observations by Jura et al. (2001). The main differences are that the OVRO maps have a higher angular resolution in which their images clearly display a central hole from 79 to 121 km s^{-1}; however, about half of the flux is missing from their observations, which can account for some of the differences between the maps. Our BIMA images contain all of the flux and exhibit more extended emission.

The intensity map integrated over 79–115 km s^{-1} reveals a bright ring within the inner 5″ in radius that peaks in the southwest quadrant and low-level extended emission elongated 10″ to the east and west (Fig. 7). The single-dish CO $J = 2 \rightarrow 1$ integrated intensity map also peaks slightly southwest from the center of the envelope and exhibits this east-west elongated feature (Bujarrabal et al. 1992). This CO peak is found opposite to the northeast peak in the mid-IR image (Fig. 7 *middle right*; Ueta et al. 2001a). The mid-IR image traces the warm dust shell, while CO probes the total column of material; hence, cold material situated in front of the warm dust shell can be absorbing the mid-IR dust emission. The optical image shows two radial plumelike extensions along P.A. $= 25°$ and 200° (Ueta et al. 2000). Gledhill & Takami (2001) suggest that these features are outflow structures causing wind interactions. Although indications of outflows appear along the direction of the plumes and along the east-west elongated feature seen in CO, the PV diagrams (with the east-west cut presented in Fig. 10) do not show any kinematic signatures of outflow structures. However, the optical plumes do coincide with the brighter clumps of CO emission along the ring.

An unusual kinematic property of HD 179821 is the fast expansion velocity of 37 km s^{-1}. In the CO catalog of evolved stars compiled by Loup et al. (1993), 86% of the O-rich sources have expansion velocities between 5 and 20 km s^{-1} with the peak distribution ranging from 10 to 20 km s^{-1}, and 92% of the C-rich sources have V_{exp} from 5 to 30 km s^{-1} with the peak occurring between 10 and 15 km s^{-1}. Fast velocities have been found in a few O-rich post-AGB stars such as OH 231.8+4.2; however, the fast outflow is mainly along the bipolar axis. The radiation pressure on silicate dust is less efficient than for carbonaceous dust; thus, the outflow velocities are expected to be smaller (Steffen & Schönberner 2000). If HD 179821 is indeed a hypergiant star, then its huge luminosity can be driving the fast spherically symmetric outflow.

3.3. *PN: NGC 7027*

Unlike the bright molecular cores commonly seen in our BIMA sample, the young PN NGC 7027 exhibits a bright molecular shell and depressed CO emission toward the core (e.g., Graham et al. 1993; Jaminet et al. 1991; Bieging et al. 1991; Masson et al. 1985). The material in the core has been ionized by the intense radiation field emanating from the hot central star ($T_{eff} \sim 198{,}000$ K; Latter et al. 2000). Around the periphery of this ionized region lies a thin layer of vibrationally excited H_2 gas that traces the PDR (Latter et al. 2000; Cox et al. 2002). The molecular gas shielded from the radiation field survives in a molecular envelope surrounding the H II region and the PDR.

The main CO envelope is consistent with a roughly spherical expanding shell. Previous authors have interpreted the geometry of the envelope to be either an oblate or prolate ellipsoidal shell, but they have either resolved out most of the emission by using an interferometer array (e.g., Masson et al. 1985; Graham et al. 1993) or lacked high resolution by using a single-dish telescope (Jaminet et al. 1991). The velocity channel maps are shown in Figure 11. The systemic velocity (26 km s^{-1}) highlights the remarkable symmetry of the envelope. The emission is very depressed at the core with a trough extending to both the northwest and southeast directions along the symmetry axis (P.A. $= -66°$, determined from the total integrated emission). This narrow emission cavity is flanked by two bright, curved ridges of emission. Surrounding these central features lies the extended, round outer envelope. Stepping to higher velocity channels, the photodissociated/photoionized hole progressively carves out the molecular gas in a southeast direction, while the two bright CO ridges curve around the central depression in a direction opposite to the advancing hole. The clumpy appearance of the ridge is mainly caused by photodissociation. At 36 km s^{-1}, the two peaks merge, and the depression appears at the southeast edge of the envelope. At about 40–42 km s^{-1}, the redshifted cap of the shell is found with a slight southeast deformation. Past the main envelope emission, high-velocity (44–49 km s^{-1}) CO gas is seen emerging from the central regions. At 46 km s^{-1}, this high-velocity CO outflow separates into two north-south blobs. The blueshifted velocities exhibit the same structures but are inverted north-south and east-west. At 10 km s^{-1} the emission is self-absorbed by the foreground gas, resulting in the depressed central hole feature.

The kinematic gas structure can be separated into three components. The first component is the general outward expansion of the envelope. The line profiles of the core and over the full envelope (Fig. 12) show the familiar double-horn structure and parabolic shape of resolved and unresolved expanding shells, respectively. The PV diagram at P.A. $= 24°$ also exhibits the characteristic oval ring pattern of an expanding shell. The PV cut along the symmetry axis shows the progression of the photodissociated/photoionized gap through the nebula as the wide, diagonal depression from blueshifted positive offsets to redshifted negative offsets. The blueshifted and redshifted emission peaks represent the shell caps at about 12 and 38 km s^{-1}. The two remaining components are the high-velocity blobs seen on the extreme blueshifted and redshifted ends of the PV diagrams and channel maps. These extreme blueshifted ($\leq$9 km s^{-1}) and redshifted ($\geq$44 km s^{-1}) blobs are best presented as blue and red contours superposed against the color image of the systemic velocity (Fig. 5, *bottom left*). These blobs are found near the central star, with the main and minor blueshifted blobs offset about 5″ north and 8″ south, respectively. The redshifted blobs are similarly offset, but transposed north-south. The general north-south alignment of these high-velocity blobs indicates that they are not aligned with the southeast-northwest photodissociated/photoionized gap. Instead, the blobs form two separate bipolar outflows: the main outflow has the northern lobe tilted toward the observer, while for the minor outflow the southern lobe is inclined toward the observer.

The near-IR color composite image of NGC 7027 taken with NIRIM (Meixner et al. 1999a) at WIYN displays the vibrationally excited H_2 in red, [Fe II] in yellow, and Brγ in blue (Fig. 5, *bottom right*). The H_2 emission shows the familiar four-lobed clover pattern interpreted by Latter et al. (2000) and Cox et al. (2002) as two limb-brightened conical shells with the northern lobe tilted toward the observer. The high-velocity components of the two limb-brightened shells are coincident with the main high-velocity blueshifted and redshifted CO blobs that are tilted in the same sense. This suggests that the high-velocity H_2 emission is tracing the PDR gas surrounding the periphery of the main CO blobs, sandwiched between the outer CO blobs and the inner ionized gas, hence forming the biconical shells. As for the minor blueshifted and redshifted CO blobs, they are coincident with the H_2 indentations found at the north-northwest and south-southeast dents in the four-lobed clover pattern. These indentations are associated with a bipolar outflow cavity found by Cox et al. (2002)

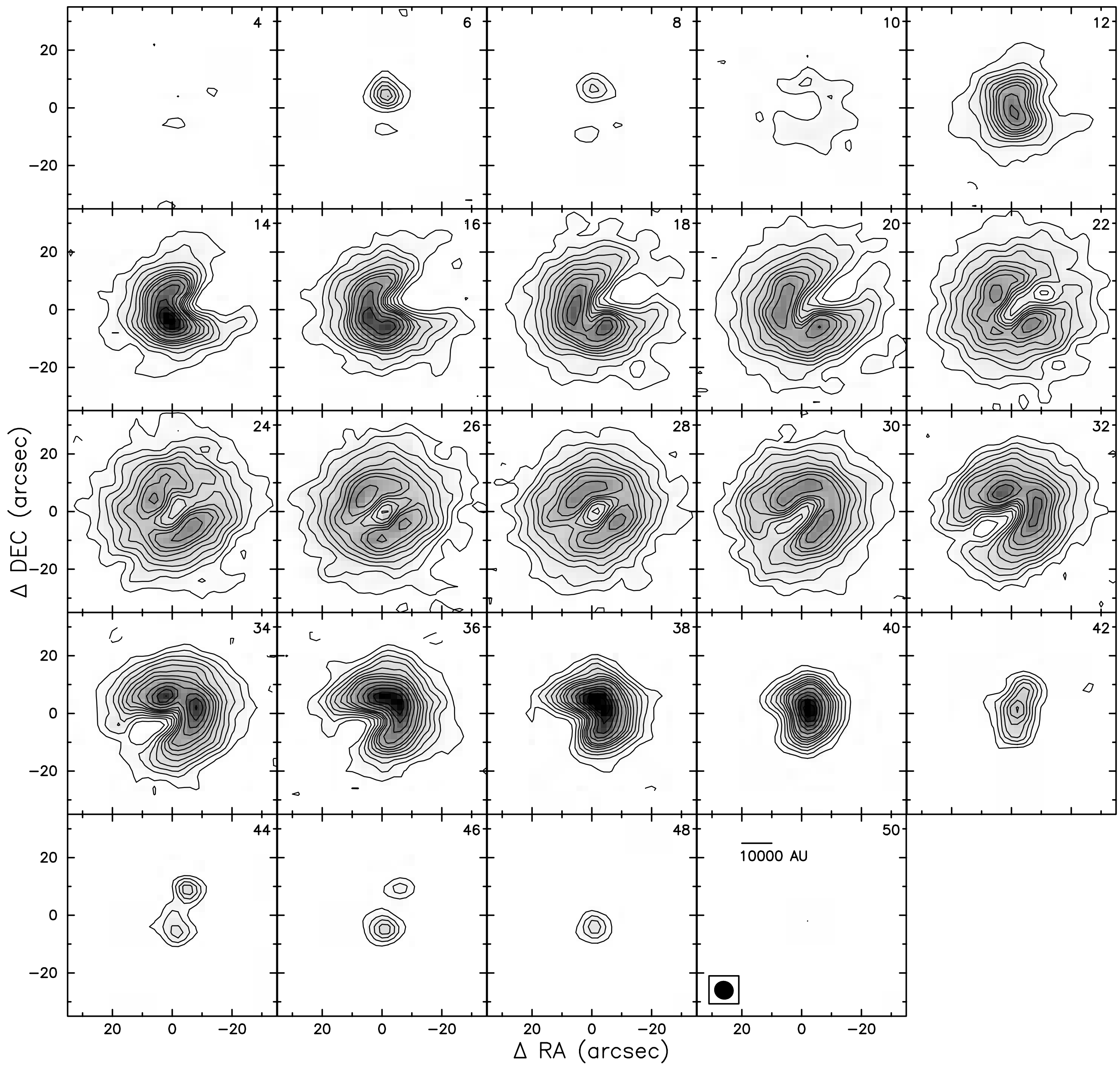

FIG. 11.— Channel maps with 2 km s^{-1} widths for NGC 7027. The first eight contour levels are in increments of 3 σ ($\sigma = 0.17$ Jy beam^{-1}), and the remaining contours are in levels of 6 σ.

and are tilted in the same sense as the minor CO blobs. The high-velocity CO blobs could be the precursors to fast low-ionization emission regions (FLIERS), which are symmetric pairs of low-ionization knots traveling at opposite directions with velocities higher than the surrounding gas in which they are embedded (e.g., Balick et al. 1998; Balick & Frank 2002). Furthermore, the narrow ends of FLIERS are pointed toward the central star, similar to the direction of the narrow ends of the biconical H_2 shells, which trace the photodissociated gas.

The two bipolar outflows and the blowout axis are highlighted in Figure 5 (*bottom left*) by the two white dotted lines and the black dotted line, respectively. These three multipolar outflows are associated with the series of openings detected in the structure of the H_2 emission that outlines outflow cavities (Cox et al. 2002). These outflows are remarkably point symmetric about the central star. Along the photodissociated/photoionized blowout axis, very high velocity gas is detected in Brγ (± 55 km s^{-1}; Cox et al. 2002) and X-ray emission ($\sim$400 km s^{-1} based on the $T \sim 3 \times 10^6$ K gas; Kastner et al. 2001). No associated high-velocity CO gas was detected along the collimated blowout axis.

3.3.1. *The Shaping of NGC 7027*

The young PN NGC 7027 exemplifies a relatively advanced stage of shaping as seen by the striking morphological transformation caused by fast outflows and radiation from the central star. It showcases many of the structures and mechanisms seen in the spherical and structured outflow classes, so here we discuss the sequence of events that may have shaped its envelope to highlight

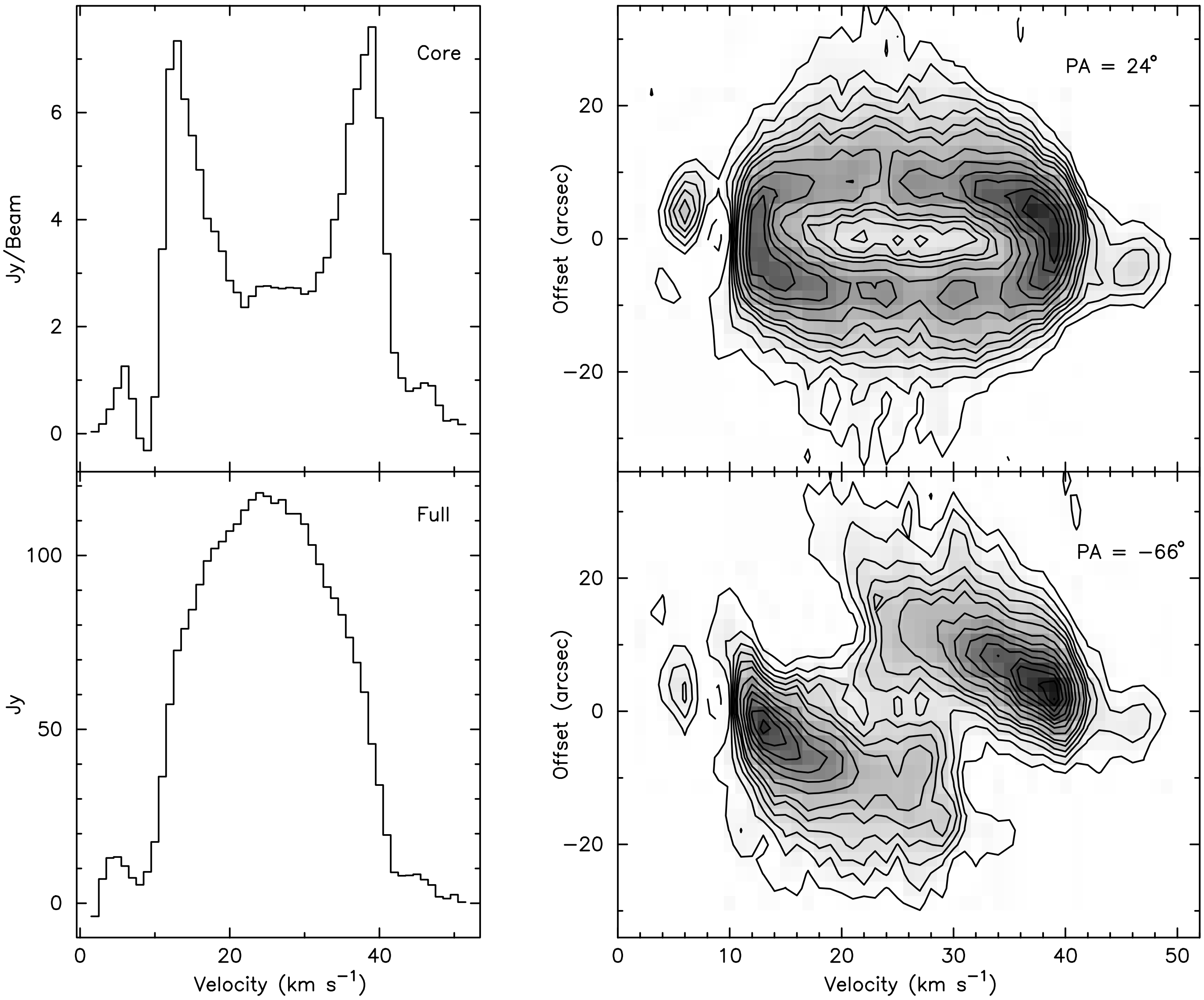

FIG. 12.—NGC 7027. *Left*: Line profile of the central core (central 5″) emission region and of the full envelope. *Right*: PV diagram cut along the bright CO ridges (P.A. = 24°) and along the collimated blowout axis (P.A. = −66°). The contour levels are similar to the channel maps.

the mechanisms behind the PN formation process. The geometry of the main envelope is roughly spherical, with a blowout along the symmetry axis and high-velocity quadrupolar outflows emerging from the central region. Figure 13 shows a cross-sectional cut of the envelope along the line of sight that shows the distinct components. The depth of the blobs within the envelope is uncertain. The observer is located on the right side facing the blue-shifted blobs. Yellow outlines the blowout region and purple outlines the region of vibrationally exited H_2 emission. The blowout axis is not aligned with the quadrupolar outflows.

The early AGB mass loss is roughly spherical and thus consistent with a typical AGB star. Concentric arcs are observed in dust; however, their molecular counterparts have not yet been detected. In its evolution into a PN, NGC 7027 likely followed the developmental scenario outlined by the general interacting stellar winds model (e.g., Balick & Frank 2002). This would explain the high-density torus and the low-density polar regions that shield the gas from being quickly photodissociated along the equator but not along the poles. Furthermore, this equatorial density enhancement would channel high-velocity wind toward the poles, consistent with the bipolar, high-velocity outflows detected in Brγ and X-ray emission. A magnetic outburst could have launched the molecular, quadrupolar outflows/blobs in directions not aligned with the blowout axis (e.g., Frank & Blackman 2004). Each mechanism can have a dramatic impact on the surrounding envelope as they become active during its evolution.

4. CLASSIFICATION BASED ON THE MORPHOLOGY AND KINEMATICS OF THE MOLECULAR GAS

The AGB, PPN, and PN archetypes show very similar features. IRC +10216, AFGL 2688, and NGC 7027 are all chemically C-rich and have high mass-loss rates, extensive gas and dust envelopes, and spherically expanding AGB envelopes. In the inner regions of AFGL 2688 and NGC 7027, fast outflow structures are seen within or projected within the extended envelope, suggesting that these outflows are relatively young, emerging at the end of the AGB stage. Optical images of these archetypes reveal concentric arcs in the outer regions surrounding the bipolar nebulae. Multiple molecular shells corresponding to the optical concentric arcs were detected by Fong et al. (2003) in IRC +10216. While no molecular arcs were detected in AFGL 2688 or NGC 7027, their larger distance compared to IRC +10216 makes it

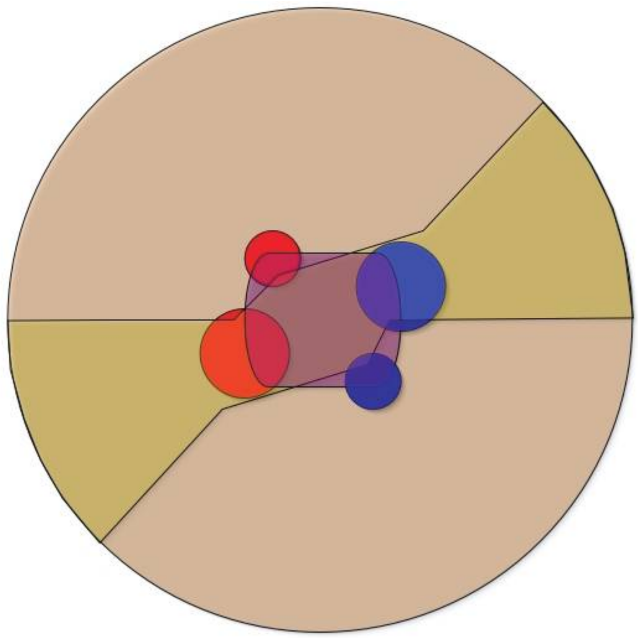

FIG. 13.— Conceptual drawing of a cross section along the line of sight of the main CO emission features of NGC 7027. North is up and earth is to the right in this diagram. The blue circles represent the blueshifted blobs of gas from Fig. 5. The red circles are the redshifted blobs. The central purple oblong region is the boundary of the H_2 emission region. The yellow double-cone region shows the blowout that is photodissociated. The pale outer circle that circumscribes all of the features is the CO envelope.

more challenging to distinguish the small contrast difference between the arc structures superposed on the bulk molecular envelope emission.

The similarities found in the these archetypes suggest that they may represent an evolutionary sequence for a class of evolved stars. The results for the remaining sources in the BIMA sample deviate from these archetypes and do not fall so neatly into another evolutionary sequence. Three of the objects, IRAS 22272+5435, HD 161796, and HD 179821, have roughly spherical envelopes that are also characterized by unusual protrusions. However, the BIMA data do not show evidence for kinematic structures that might shape these protrusions. The optical morphologies for these sources were classified as SOLE by Ueta et al. (2000), suggesting that the circumstellar dust envelope is optically thin. The two remaining sources, 89 Her and Mira, have hints of disk rotation in their kinematics and additional independent evidence for a disk surrounding a binary system. These deviations from the archetypes suggest that there may be more than one class, possibly three distinct morphological and kinematical classes in the BIMA sample.

The BIMA sample alone is too small to make any firm conclusions about object classification. However, it has inspired us to search the literature for similar molecular mapping observations in order to produce a sufficiently enlarged sample to make an object classification meaningful.

4.1. *Enlarged Sample from Literature Search*

We have searched the literature and have selected additional sources based on the following two criteria:

1. The circumstellar envelope is mapped and spatially and kinematically resolved in the CO line emission so that it could be classified and measured in size.

2. The objects are studied well enough to have well-determined stellar effective temperature ($T_{\rm eff}$) and luminosity (L) values and thus be reliably placed on the H-R diagram.

The additional sources from the literature have been combined with the BIMA survey sample in Table 6, which lists properties of the star ($T_{\rm eff}$, L, D) and of the molecular envelope ($V_{\rm exp}$, R, t, $\dot{M}$, f) for 38 objects. The expansion velocity, $V_{\rm exp}$, represents the simple expanding component of the envelope; the structured outflow component of a subset of sources is discussed below. The radius of the envelope, R, is the outer radius of the CO emission as measured in the CO emission maps published here or in other papers. We convert R into a physical scale size using the distance to the source. The timescale, t, is derived simply by dividing the CO radius by the expansion velocity. This timescale is a lower limit to the formation time of the molecular envelope because the outer CO radius is a lower limit to the real outer radius of the envelope. Photodissociation by the ISRF will limit the size of the molecular envelope (e.g., Mamon et al. 1988). This enlarged sample is plotted on the H-R diagram (Fig. 14), and the individual sources are labeled with their name and an identification number (arranged according to evolutionary age; see Table 6), which will be used to represent the sources in the following plots. C-rich and O-rich sources are equally represented in the sample and identified by color in the H-R diagram. The enlarged sample has a bias toward sources that are bright and extended and show interesting structures at other wavelengths since these type of sources have a higher tendency to be mapped, thus there may be a disproportionate number of bipolar nebulae.

4.2. *Three Classes*

Our larger sample exhibits many features similar to those observed in our BIMA survey. Here we broadly define three classes based primarily on the molecular morphology and kinematic structure of the gas traced by CO. For those objects that display multiple features, we use the most striking and highest order structure to classify them. The morphology is wavelength specific since they trace different components of the envelope. Objects that appear spherical in molecular gas may appear bipolar in the optical/IR, but the latter usually probes only a small fraction of the circumstellar material close to the star, while CO traces the entire envelope. We use the CO maps and classify such objects as spherical types. Figure 14 displays how each object in the enlarged sample is identified as one of the following three classes.

1. Spherical, elliptical, or shell sources show simple expanding envelopes with constant outflow velocities. IRC +10216 is the classic example of such a source. We include objects with detached shells and thin detached shells in this category. Detached shells are formed after the termination of AGB mass loss when the inner edge of the circumstellar envelope coasts away from the central star. Thin detached shells are likely formed through episodic mass loss modulated by thermal pulses (Olofsson et al. 2000). A small subgroup of carbon stars undergoes this phenomenon, with TT Cyg being the archetype.

2. Disk sources show compact, sometimes disklike molecular structures with evidence for rotation along the disk. These sources usually exhibit a slow AGB expansion velocity and low mass-loss rates and reside in binary systems. Lower expansion velocities and smaller binary separation distances will increase the influence of the secondary over the primary's AGB wind. Hydrodynamic models of detached binary systems show that the secondary acts to redirect the radially outflowing wind of the primary to (*a*) rotate around the primary in an equatorial disk structure and (*b*) form an

TABLE 6
Properties of the Molecular Envelope Classification Sample

ID	Name	$T_{\rm eff}$ (K)	L ($L_\odot$)	D (pc)	$V_{\rm exp}$ (km s^{-1})	R (arcsec)	R (cm)	t (yr)	$\dot{M}$ ($M_\odot$ yr^{-1})	f	References
1	S Cep	1900	7300	340	23	19	9.7E+16	1300	1.5E−06	1	1, 2
2	IRC +10216	2000	18000	150	14	190	4.3E+17	9700	3E−05	1	3, 4, 5, 6
3	V Cygni	2000	6200	430	11.3	8	5.2E+16	1400	1.6E−06	1	7
4	OH 26.5+0.6	2000	20000	1400	15	10	2.1E+17	4400	5.3E−04	1	6, 8, 9, 10, 11
5	T Dra	2100	6300	610	14	13	1.2E+17	2700	1.2E−06	1	1, 12
6	V CrB	2400	5300	630	8	7	6.6E+16	2600	6E−07	1	1, 12
7	CL Mon	2500	7500	770	25	10	1.2E+17	1500	2.2E−06	1	1, 12
8	IRC +40540	2500	9000	700	16	30	3.2E+17	6200	1.5E−05	1	1, 2, 6, 13
9	V Hydra	2650	14000	380	10	10	5.7E+16	1800	4E−05	1	14, 15, 16
10	Y CYn	2700	4400	220	10	10	3.3E+16	1000	1.5E−07	1	1, 2
11	U Cam	2700	7000	430	23	7	4.5E+16	620	1E−05	1	17, 18
12	CIT 6	2800	10000	400	18	50	3.0E+17	5300	6E−06	1	19
13	OH 231.8+4.2	2900	10000	1500	40	8	1.8E+17	1400	2.3E−04	1	20, 21, 22
14	TT Cygni	3000	2800	510	12.6	35	2.7E+17	6700	1E−05	1	23, 24
15	UU Aur	3000	6900	260	12	10	3.9E+16	1000	3.5E−07	1	1, 12
16	RY Dra	3000	10000	490	13	10	7.4E+16	1800	3E−07	1	1, 12
17	Mira	3000	8000	130	5	26	5.1E+16	3200	1E−07	1	6, 25, 26
18	RV Bootis	3200	8100	390	2.8	4	2.6E+16	3000	4E−08	1	27, 28
19	X Her	3300	9200	140	3	6	1.3E+16	1400	9E−08	1	29, 30, 31
20	Frosty Leo	3850	2700	3000	20	6	2.7E+17	4300	1.2E−04	1	21, 32
21	IRAS 22272+5435	4850	8300	1700	9	14	3.6E+17	13000	2E−05	1	21, 33, 34
22	IRC +10420	6100	700000	5000	35	12	9.0E+17	8200	5E−04	1	21, 35
23	HD 179821	6750	600000	5600	37	10	8.4E+17	7200	4.8E−03	1	21, 36, 37, 38
24	AFGL 2688	7000	25000	1200	15	20	3.7E+17	7800	2.0E−04	1	21, 39, 40
25	HD 161796	7000	3000	1000	8	8	1.3E+17	5100	1.4E−04	1	36, 41
26	89 Her	7000	9000	1000	8	12	1.9E+17	7400	4E−06	1	21, 42, 43, 44
27	HD 56126	7250	6700	2400	11	6	2.2E+17	6200	5E−06	1	45
28	Red Rectangle	10000	1000	380	0.4	2	1.4E+16	11000	2E−07[a]	0.5	42, 46, 47, 48, 49
29	M2-56	20000	5000	2100	8	8	2.5E+17	10000	2.3E−05	1	21, 50
30	M1-92	20000	10000	2500	8	2	9.4E+16	3700	2.2E−04	0.82	21, 39, 51, 52, 53
31	M2-9	25000	550	1000	7	6	9.0E+16	4100	6.4E−07	0.10	21, 39, 54, 55
32	IRAS 21282+5050	30000	5300	2000	16	35	1.1E+18	21000	6E−05	0.96	19, 47, 56, 57
33	AFGL 618	30000	30000	1700	20	30	7.7E+17	12000	2E−04	0.99	19, 39, 47, 58, 59
34	M1-16	34000	120	1800	11	25	6.8E+17	19000	2E−05	0.98	60, 61
35	BD +30 3639	40000	6600	1500	50	4	9.0E+16	570	1E−04	0.012	62, 63, 64, 65
36	NGC 7027	200000	10000	1000	16	40	6.0E+17	12000	4E−04	0.85	21, 47, 66, 67, 68
37	Ring	120000	1000	920	27	50	6.9E+17	8100	2E−04[a]	0.47	47, 69, 70
38	Helix	123000	120	200	29	500	1.5E+18	16000	1E−04[a]	0.15	71, 72, 73

[a] These mass-loss rates are estimates that equal the total mass detected in these sources divided by the timescale over which this mass was lost from the star. The total mass includes molecular, atomic, and ionized gas masses.

References.—(1) Neri et al. 1998; (2) Schöier et al. 2002; (3) Fong et al. 2003; (4) Groenewegen 1997; (5) Groenewegen & Ludwig 1998; (6) Kholopov 1985; (7) Bieging & Wilson 2001; (8) Fong et al. 2002; (9) Justtanont et al. 1996; (10) Lorenz-Martins & de Araujo 1997; (11) van Langevelde et al. 1990; (12) Schöier & Olofsson 2001; (13) Groenewegen et al. 1998; (14) Hirano et al. 2004; (15) Knapp et al. 1997; (16) Knapp et al. 1999; (17) Lindqvist et al. 1999; (18) Schöier et al. 2005; (19) Meixner et al. 1998; (20) Alcolea et al. 2001; (21) Bujarrabal et al. 2001; (22) Sanchez Contreras et al. 1997; (23) Jørgensen et al. 2000; (24) Olofsson et al. 2000; (25) Feast 1996; (26) Josselin et al. 2000; (27) Bergman et al. 2000; (28) Kerschbaum et al. 1997; (29) Dyck et al. 1996; (30) Kahane & Jura 1996; (31) Nakashima 2005; (32) Castro-Carrizo et al. 2005; (33) Hrivnak 1995; (34) Szczerba et al. 1997; (35) Castro-Carrizo et al. 2001b; (36) Hrivnak et al. 1989; (37) Jura et al. 2001; (38) Reddy & Hrivnak 1999; (39) Calvet & Cohen 1978; (40) Skinner et al. 1997; (41) Meixner et al. 2002; (42) Alcolea & Bujarrabal 1991; (43) Alcolea & Bujarrabal 1995; (44) Waters et al. 1993; (45) Meixner et al. 2004; (46) Bujarrabal et al. 2003; (47) Fong et al. 2001; (48) Kelly & Latter 1995; (49) Knapp et al. 1995; (50) Castro-Carrizo et al. 2002; (51) Bujarrabal et al. 1998a; (52) Bujarrabal et al. 1998b; (53) Castro-Carrizo et al. 2001a; (54) Schwarz et al. 1997; (55) Zweigle et al. 1997; (56) Crowther et al. 1998; (57) Meixner et al. 1997; (58) Bujarrabal et al. 1988; (59) Bujarrabal et al. 1992; (60) Huggins et al. 2000; (61) Sahai et al. 1994; (62) Bachiller et al. 1991; (63) Bachiller et al. 2000; (64) Li et al. 2002; (65) Bachiller et al. 1992; (66) Graham et al. 1993; (67) Latter et al. 2000; (68) Liu 1997; (69) Bachiller et al. 1989; (70) Cahn 1984; (71) Rodríguez et al. 2002; (72) Young et al. 1999; (73) Speck et al. 2002.

accretion disk around the secondary (Mastrodemos & Morris 1998, 1999). The Red Rectangle is the archetype of this class. We include 89 Her and Mira as candidates for this class because they exhibit many features of this class including suggestive, albeit not conclusive, evidence for rotating disks.

3. Structured outflow sources show bipolar or multipolar outflow structures with tori expanding at the AGB envelope velocities. These high mass-loss rate objects possess structures with velocities higher than the expanding tori and the surrounding AGB envelope. These structures are apparent in the molecular distribution of gas in the PPN AFGL 2688 and young PN NGC 7027. However, in the more evolved PNe, like the Ring Nebula and the Helix Nebula, often only the remnant molecular expanding disk is seen alone with evidence for the bipolar/multipolar structures in ionized gas.

4.3. *H-R Diagram*

The populated H-R diagram (Fig. 14) reveals several trends with evolutionary stage. First, there is a clear division of morphological/kinematical types with evolutionary age. The predominately spherical/elliptical/shell types found on the AGB are in stark contrast to the primarily structured outflow type seen

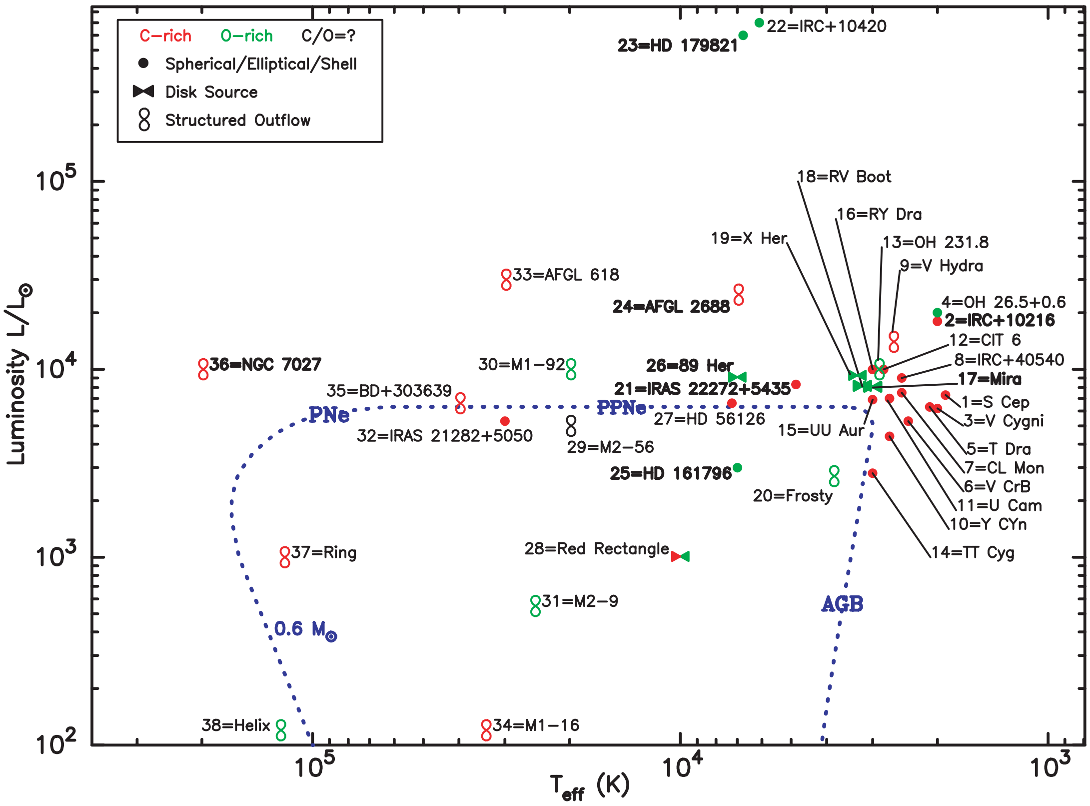

FIG. 14.—Distribution of the enlarged sample of sources plotted in an H-R diagram based on the stellar properties listed in Table 6. The labeled symbols indicate the classification based on the molecular gas morphology and kinematics, and the color represents the chemistry ("C-rich" is carbon-rich, "O-rich" is oxygen-rich, and "C/O?" is unknown chemistry). The names of the sources are adjacent to or have a line drawn to their symbol. The source ID numbers are listed in Table 6. The blue dashed line shows the approximate evolutionary path for an intermediate-mass star destined to become a 0.6 $M_\odot$ white dwarf.

on the PN stage, while a mixture of types are found on the transitional PPN stage. This morphological/kinematical trend is seen for both C- and O-rich sources, implying no dependence on chemistry. The fact that most of the structured outflow sources are found at $T_{\rm eff} > 10{,}000$ K suggests that structured outflows emerge after the AGB stage. However, structured outflows are detected as early as $T_{\rm eff} = 2650$ K from extreme AGB stars such as Frosty Leo (Castro-Carrizo et al. 2005), OH 231.8+4.2 (Alcolea et al. 2001), and V Hydra (Hirano et al. 2004). These three unusual AGB sources exhibit high-velocity bipolar outflows with central expanding disks/tori, high mass-loss rates, and evidence for binary companions. Theoretical studies indicate the importance of binary interactions in shaping asymmetric PNe. Disks may form around the companion through accretion of the dense AGB wind (Mastrodemos & Morris 1998). During the superwind phase, the conditions are more favorable for the formation of an accretion disk since the AGB wind is intensive and slow (Soker 2005). In Figure 14, a small group of disk sources are clustered at the tip of the AGB, which may support this claim. It appears more than coincidental that the three extreme AGB stars with structured outflows are also found there. If the mass accretion rate is high enough, then two fast collimated winds can be powered through magnetocentrifugal launching (Frank & Blackman 2004). The structured outflow seen in the AGB stars OH 231.8+4.2, V Hydra, and Frosty Leo may be blown via a combination of these collimating processes. These structured outflow sources have high mass-loss rates and consequently high opacities that easily mask the accompanying rotating disk of material created by the binary interaction. Thus, the structured outflow sources may be the high-mass counterparts to the disk sources that are more visible due to their lower mass-loss rates and low expansion velocities and that show more kinematical signatures from the rotational component.

Second, disk sources appear only at intermediate to low luminosities and at low $T_{\rm eff}$ (<10,000 K; Red Rectangle). As shown in Table 6, these sources tend to have lower expansion velocities, lower mass-loss rates, and lower molecular masses. Thus, it is possible that their molecular gas is completely photodissociated and no longer detectable in CO emission when the star evolves to higher $T_{\rm eff}$, and thus excluded from our sample. The reason that such low-mass sources have any detectable CO emission may be due to the fact that it resides in a long-lived disk as suggested for several faint CO line sources by Jura & Kahane (1999) and shown quite clearly for the Red Rectangle by Bujarrabal et al. (2003, 2005). They argue that the binarity of some of these systems, e.g., the Red Rectangle, and perhaps all of them, caused mass transfer that resulted in the creation of a long-lived disk. These disk sources appear to be O-rich, with the Red Rectangle showing signs of both types of chemistries, suggesting a dependence on chemistry for this class; however, the numbers in the class are too small to make this a firm conclusion.

Third, there appears to be a paucity of PNe in the H-R diagram. While part of this deficiency may be related to the lack of quality CO maps of PNe, another factor is the increasing photodissociative effects of the molecular envelope by the hot central star. The result is that most PNe do not have enough detectable molecular gas that survives this process (see further discussion below). Furthermore, some stars have mass-loss rates that are too low at the tip of the AGB phase to be detectable during the PN stage.

Fourth, IRAS 21282+5050 appears to be the only PN in our survey that lacks structured outflows. Soker (2004) suggested that most spherical PNe do not show signatures of a superwind, since binary interaction models favor superwind conditions to transition to asymmetry. IRAS 21282+5050 is consistent with these models since no clear evidence of a superwind was found (Meixner et al. 1998). Moreover, recent surveys have detected more PNe with binary systems (e.g., De Marco et al. 2004), which is consistent with the high numbers of PN structured outflow sources in the sample.

Finally, the two high-luminosity outliers, HD 179821 and IRC +10420, which have been classified by some authors as PPNe, appear to be yellow hypergiants (Jura et al. 2001; de Jager 1998). While these sources share similar observational properties as PPNe, the hypergiants show very high $V_{\rm exp}$ and mass-loss rates that will appear as the outliers on some of the plots discussed in § 5.

5. THE EVOLUTION OF THE MOLECULAR ENVELOPE

The trends revealed on the H-R diagram (Fig. 14) indicate an evolution of the molecular envelope caused by radiative effects of the fast evolving $T_{\rm eff}$ and dynamical effects of the fast, collimated winds. In order to further investigate the evolution of the molecular envelope, we have plotted the stellar and circumstellar envelope parameters against each other. In the following two subsections we discuss the remaining plots and their implications for (1) photodissociation of the molecular envelope and (2) the kinematical evolution of the envelope.

5.1. *Photodissociation of the Molecular Envelope*

AGB mass loss creates a molecular envelope that will eventually be photodissociated and photoionized as the central star evolves to hotter effective temperatures. In addition, the dynamical evolution of the envelope from the interaction of fast winds with the slower AGB wind may also dissociate and ionize the envelope through shocks. *ISO* observations and analysis of the atomic fine-structure lines have shown that photodissociation dominates the evolution of the molecular gas into neutral atomic gas in CSEs (Fong et al. 2001; Castro-Carrizo et al. 2001a). Moreover, the CO line emission study of 100 PNe by Huggins & Healy (1989) reveals only 19 detections with a trend of decreasing molecular mass fraction with radius of the nebula, both of which support photodissociation of the molecular gas with evolution.

The top panel of Figure 15 shows how the mass-loss rates of the sample objects compare with the effective temperatures of their central stars. This plot resembles the H-R diagram figure in that there are more objects with molecular gas at lower effective temperatures than at higher effective temperatures. Moreover, the AGB stars at lower effective temperatures cover a wide range of mass-loss rates (10^{-7} to 10^{-3} $M_\odot$ yr^{-1}). With increasing $T_{\rm eff}$, the mass-loss rate range narrows to the higher mass-loss rate regime; thus, only the highest mass-loss rate objects retain a significant fraction of their molecular gas into the PN phase. In addition, these PNe are all structured outflow sources that have dense expanding tori that act to protect the molecular gas through self-shielding. Such a trend is expected if photodissociation plays a major role in the evolution of the molecular envelope. This trend also explains the lack of disk sources at higher effective temperatures in our sample. All of the disk sources are found at lower mass-loss rates; hence, we would not expect the low-mass molecular disk to survive as the source evolves to hotter effective temperatures.

The bottom panel of Figure 15 displays the fraction of the total gas mass that is molecular in comparison with the effective temperature of the central star. The total gas mass equals the sum of the ionized, neutral atomic, and molecular gas masses found within

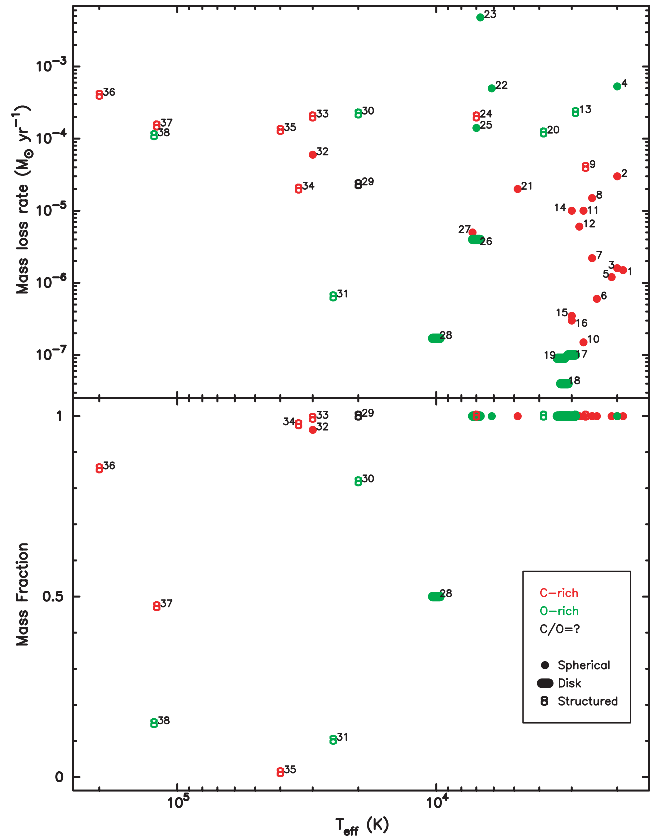

Fig. 15.—*Top*: Mass-loss rate vs. effective temperature for the enlarged sample (source ID numbers are listed in Table 6). *Bottom*: Molecular mass fraction vs. effective temperature. A molecular mass fraction of $f = 1$ means that the envelope is essentially all molecular. The ID numbers of sources with $f = 1$ (ID $\leq$ 27) were suppressed in the plots to reduce confusion.

the molecular envelope. The fraction of molecular gas mass equals the molecular gas mass divided by the total gas mass (Table 6). A mass fraction of 1 means that all of the gas is molecular. All of the objects with a $T_{\rm eff} < 10{,}000$ K have a mass fraction of 1, with the sole exception of M2-56 (29). The maximum mass fraction appears to decrease with increasing $T_{\rm eff}$ and evolutionary age. For example, AFGL 618 (33) is close to 1, whereas the fraction drops to less than 0.9 for NGC 7027 (36) and to less than 0.2 for the Helix (38), which has a lower $T_{\rm eff}$ than NGC 7027 as expected for an evolved PN that is on the cooling track (Fig. 14). However, there is a range in mass fractions over $T_{\rm eff}$ because of the mass-loss rate effect. Lower mass-loss rate objects, such as the Red Rectangle (28) and M2-9 (31), will become photodissociated at lower $T_{\rm eff}$ and thus have a lower mass fraction at lower $T_{\rm eff}$ than higher mass-loss rate objects that will always reside in the higher mass fraction region.

For all objects, the left panel of Figure 16 reveals a very good correlation between envelope radii and mass-loss rates. Objects with higher mass-loss rates are found to have larger radii. In the case of AGB stars, this tight relation between mass-loss rate and envelope radius supports the understanding that the ISRF limits the size of the outer envelope through external photodissociation and that mass-loss rate determines the effectiveness of the ISRF photodissociation process (Mamon et al. 1988). Theoretical envelope radii versus mass-loss rate curves from Mamon et al. (1988) agree reasonably well with the AGB stars possessing typical mass-loss rates in our sample, i.e., the C-rich spherical/elliptical sources. Our AGB star sample appears to be clustered closer to the

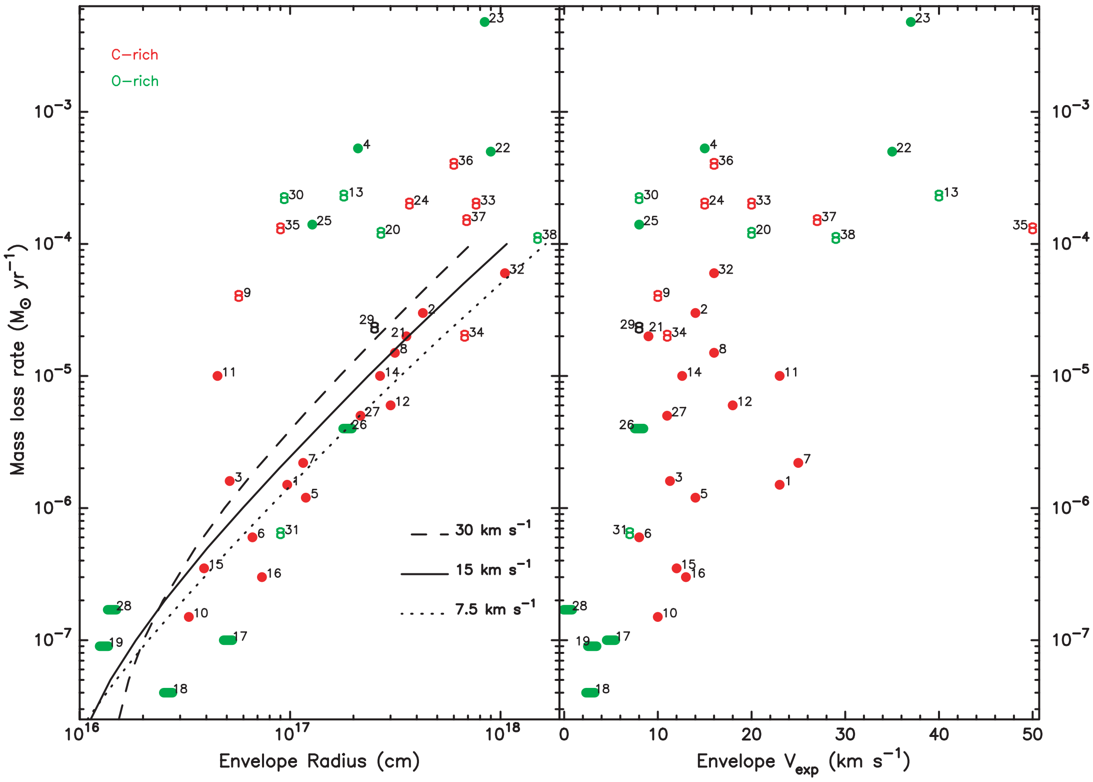

FIG. 16.—*Left*: Mass-loss rate vs. envelope radius for the sample in Table 6. The lines are theoretical expectations for this relation from Mamon et al. (1988) for three different expansion velocities, 30, 15, and 7.5 km s^{-1}. *Right*: Mass-loss rate vs. envelope expansion velocity for the sample in Table 6. For both plots, source ID numbers are listed in Table 6.

7.5 km s^{-1} curve even though the AGB stars have velocities between 8 and 25 km s^{-1} (Fig. 16, *right panel*). The offset may indicate that the measured radii are too large for the stated mass-loss rate. However, observational bias would most likely underestimate the full extent of the envelopes because of the lack of sensitivity to the low surface brightness edge of the envelope. Alternatively, the mass-loss rates may be underestimates for these sources. In any case, we do not consider this clustering at 7.5 km s^{-1} to be a major discrepancy with the Mamon et al. (1988) theory because the envelope radii and mass-loss rates were derived from a heterogeneous selection of values from the literature and not from self-consistent models of the sources.

In addition to the AGB stars, several of the PNe fall within the expectations of the Mamon et al. (1988) curves. For the PN, the central star's photodissociation plays a more important role than the ISRF. In addition, the radius of the envelope for a PN is determined more by the age of the nebula because the nebula is simply coasting away from the central star. However, despite these differences, the result is similar to that for the AGB stars. We might expect a relationship between the radius of the CO emission and the mass-loss rate because the higher the mass-loss rate, the older the PN can be detected in CO. In addition, higher mass-loss rate PPNe will create more massive molecular envelopes that can better shield themselves from the UV photons from the central star.

Although all of the objects follow an overall trend where higher mass-loss rates will enhance the molecular self-shielding from external photodissociation, thus yielding larger envelope sizes, there are significant deviations from the Mamon et al. (1988) curves at the highest and lowest ends of the mass-loss rate range. At the highest mass-loss rates, there are two physical explanations for the deviations. The two hypergiant stars, IRC +10420 (22) and HD 179821 (23), have extreme mass-loss rates for their envelope size because of their larger luminosities and different stellar wind processes. Of the remaining objects, most are post-AGB objects, which are typically structured outflow sources, or tip-of-the-AGB sources like OH 26.5+0.6 (4) and OH 231.8+4.2 (13). Most of these sources have recently experienced a superwind, which is a dramatic increase in mass-loss rate at the end of an AGB star's life (e.g., Meixner et al. 1997, 1998, 2004; Fong et al. 2002). This higher mass-loss rate is detected in the CO lines; however, its duration has been too short to impact the envelope radius. Here it is important to note that the Mamon et al. (1988) models are calculated assuming a steady state mass-loss rate over the time of the envelope's interaction with the ISRF.

At the lowest mass-loss rate end, we find that the disk sources have a more random distribution between their estimated mass-loss rates and their respective envelope radii. If these disk sources have gravitationally bound disks, as demonstrated for the Red Rectangle (Bujarrabal et al. 2005), then the mass-loss rate is meaningless because the CO in these systems is not tracing an AGB mass-loss wind. Indeed, the envelope radii and disk masses will be determined by the properties of the central stars and disk evolution.

5.2. *Kinematical Evolution of the Envelope*

While photodissociation appears to play the major role in destroying the molecules, the dynamical interaction of multiple winds is a significant agent in the morphological transformation of the nebula from spherical to nonspherical geometries. The simple expansion of the slow, spherical AGB wind is the default assumption for the kinematics of the molecular envelope. Below we discuss how the structured outflow and disk sources deviate from the simple expansion assumption.

The right panel of Figure 16 shows a weak correlation between the mass-loss rate of the source and the expansion velocity

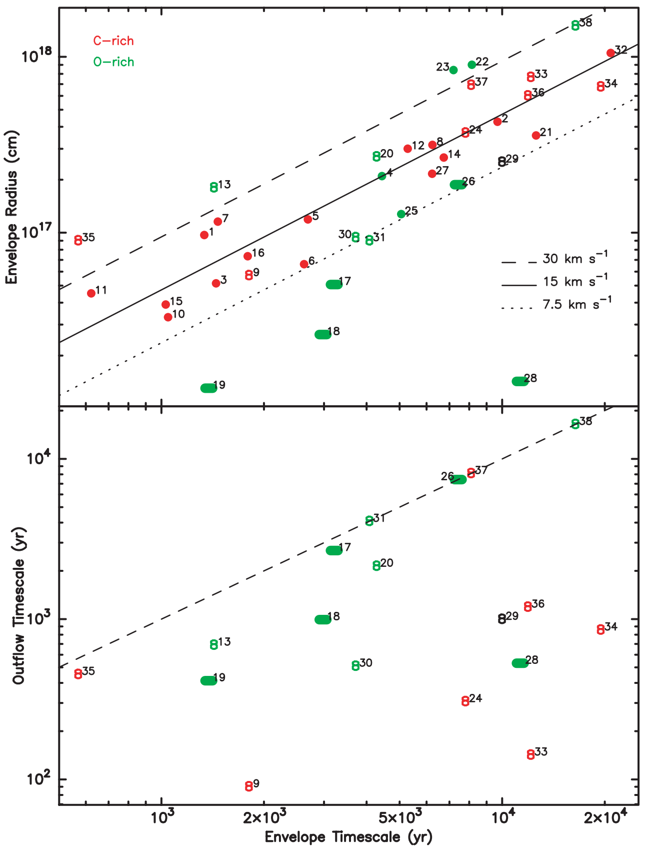

FIG. 17.— *Top*: Plot of envelope radius vs. envelope timescale for the enlarged sample of Table 6 (source ID numbers are listed in Table 6). Three lines showing the relation between envelope radius and envelope timescale expected for constant velocity outflows of 30, 15, and 7.5 km s^{-1} are also shown. *Bottom*: Timescale to create the outflow structure vs. the timescale of the expanding envelope structure (source ID numbers are listed in Tables 6 and 7).

of the ejected envelope. At the highest velocity end, the two hypergiants IRC +10420 (22) and HD 179821 (23) have correspondingly higher mass-loss rates. At the lowest velocity end, the disk sources have the lowest mass-loss rates. Most of the sources, however, have velocities in the typical range of 8–30 km s^{-1} and cover a wide range of mass-loss rates. Fitting a single power law to the whole data set results in $\dot{M} \propto V_{\rm exp}^{3.1}$ with a correlation coefficient of 0.36, indicating a weak correlation. The power-law exponent, 3.1 ± 0.7, agrees within its errors with the power-law exponent (2.5) derived by Schöier & Olofsson (2001). They found a stronger correlation (coefficient = 0.78) in part because their sample included only AGB stars for which they derived mass-loss rates based on self-consistent radiative transfer models. In contrast, our approach took reported values from various sources in the literature for a sample covering the AGB to PN phases. In addition, our sample has a larger proportion of structured outflow sources that appear, in general, to have significantly higher mass-loss rates compared to the spherical/elliptical expanding sources for the typical envelope $V_{\rm exp}$ range (Fig. 16, *right panel*). The result is a larger spread of mass-loss rates for a given envelope $V_{\rm exp}$ range.

The top panel of Figure 17 shows the envelope radius versus the envelope timescale, which is the lower limit to the formation time of the molecular envelope since photodissociation from the ISRF will limit the size. Three lines of constant velocities 30, 15 and 7.5 km s^{-1}, which correspond to the velocities assumed in

TABLE 7

ADDITIONAL PROPERTIES OF THE STRUCTURED OUTFLOW (SO) AND DISK CLASSES

ID	Name	Class	D (pc)	$V_{\rm outflow}$ (km s^{-1})	$R_{\rm outflow}$ (arcsec)	$R_{\rm outflow}$ (cm)	$t_{\rm outflow}$ (yr)
9.........	V Hydra	SO	380	300	15	8.6E+16	90
13.......	OH 231.8+4.1	SO	1500	300	29	6.5E+17	690
17.......	Mira	Disk	130	6	26	5.1E+16	2700
18.......	RV Bootis	Disk	390	8.4	4	2.6E+16	990
19.......	X Her	Disk	140	10	6	1.3E+16	410
20.......	Frosty Leo	SO	3000	40	6	2.7E+17	2100
24.......	AFGL 2688	SO	1200	136	7	1.3E+17	310
26.......	89 Her	Disk	1000	8	12	1.9E+17	7400
28.......	Red Rectangle	Disk	380	8.5	2	1.4E+16	530
29.......	M2-56	SO	2100	200	20	6.3E+17	1000
30.......	M1-92	SO	2500	70	3	1.1E+17	510
31.......	M2-9	SO	1000	7	6	9.0E+16	4100
33.......	AFGL 618	SO	1700	340	6	1.5E+17	140
34.......	M1-16	SO	1800	30	3	8.1E+16	860
35.......	BD +30 3639	SO	1500	63	4	9.0E+16	450
36.......	NGC 7027	SO	1000	22	5	8.3E+16	1200
37.......	Ring	SO	920	27	50	6.9E+17	8100
38.......	Helix	SO	200	29	500	1.5E+18	16000

the Mamon et al. (1988) models, enclose most of the sources. The highest velocity sources, such as IRC +10420 (22), HD 179821 (23), and OH 231.8+4.2 (13), appear just above the 30 km s^{-1} line but do not appear as a significant deviation. The disk sources, however, appear significantly below the 7.5 km s^{-1} line; i.e., the envelope timescale is much longer in comparison to the envelope radius. The velocities in these disk sources are very low, so low in fact that the envelope could be gravitationally bound and the envelope timescale loses meaning.

Table 7 lists the additional kinematical properties of all of the sources that have been classified as structured outflow sources and disk sources because they have velocity components other than simple expansion. The outflow timescale ($t_{\rm outflow}$) equals the outflow size ($R_{\rm outflow}$), which is the average radius for the structured outflows, divided by the outflow velocity ($V_{\rm outflow}$). The bottom panel of Figure 17 and Figure 18 plot the outflow properties against their corresponding simple expansion components that were listed in Table 6. For all three properties, the straight line on the plots shows where the sources would lie if their outflow properties were identical to their expansion properties, which is where all of the spherical/elliptical expansion sources are located. The structured outflow sources differ in their behavior from the disk sources, and we discuss them separately below.

The structured outflow sources are typically characterized by bipolar or multipolar outflows in addition to the simple expansion. The outflow velocities are always comparable to or higher than envelope expansion velocities (Fig. 18, *top panel*). However, the outflow radii are larger than, smaller than, or the same as the envelope radii (Fig. 18, *bottom panel*). In all cases except the three PNe for which the molecular gas only traces the expanding torus, the outflow timescales are always shorter than the envelope timescales (Fig. 17, *bottom panel*). This last result clearly suggests that the structured outflows postdate the more slowly expanding AGB wind and constrains the onset of structured outflows to the end of the AGB or the post-AGB phase of stellar evolution.

The disk sources are characterized by possible rotation in addition to possible expansion. For these sources, the outflow velocity is fairly comparable to the expansion velocity (Fig. 18,

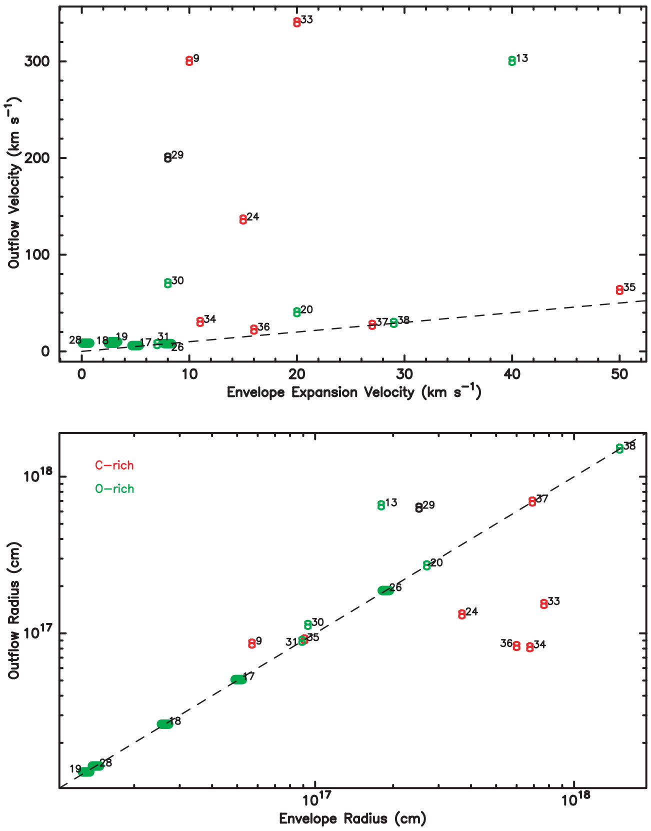

FIG. 18.—*Top*: Velocity of the structured outflow component vs. the velocity of the simply expanding envelope component. *Bottom*: Radius of the outflow structure vs. radius of the expanding envelope structure. For both plots, source ID numbers are listed in Tables 6 and 7.

top panel), the sizes of the envelopes are essentially the same (Fig. 18, *bottom panel*), and the outflow timescale is the same as or lower than the expansion timescale (Fig. 17, *bottom panel*). However, as previously mentioned, the timescales for the disk sources do not have the same meaning as for the structured outflow sources, and these differences with the structured outflow sources serve mainly to emphasize that they are indeed a different class of objects. In fact, our labeling of an outflow and expansion velocity for the disk sources is probably misleading. Bujarrabal et al. (2005) show that the CO emission in the Red Rectangle, which has a central peak and faster velocity wings, is partially resolved into three components: (1) a rotating disk with angular momentum conservation, (2) a disk in Keplerian rotation, and (3) an outflow. If all of the disk source velocity structures are explainable in the same way, then the different velocities are all related to the disk structure and not independent winds as we find in the structured outflow sources.

6. CONCLUSIONS

We summarize our conclusions as follows:

1. We present new high-resolution spatial and kinematic ^{12}CO $J = 1 \rightarrow 0$ maps of the full molecular envelopes of eight evolved stars: IRC +10216, Mira, AFGL 2688, IRAS 22272+5435, HD 161796, 89 Her, HD 179821, and NGC 7027.
2. The high-resolution CO maps display features similar to and/or complementary with images taken at optical, near-IR, and mid-IR wavelengths that trace different components of the envelope, generally much closer to the central star.
3. Drawing from the literature, we augmented our BIMA survey sample to 38 well-studied sources with CO emission maps. We classified this sample of sources based on the kinematics and morphologies of the CO emission into three types: spherical/elliptical/shell sources (e.g., IRC +10216), disk sources (e.g., the Red Rectangle), and structured outflow sources (e.g., AFGL 2688 or NGC 7027).
4. Confirming the studies of Fong et al. (2001), Castro-Carrizo et al. (2001a), and Huggins & Healy (1989), we find that photodissociation dominates the evolution of the molecular gas into neutral atomic gas in CSEs as an object evolves from the AGB to PN stages. NGC 7027 exemplifies a relatively advanced stage of shaping caused by fast outflows and radiation from the central star.
5. We find significant differences between the three morphological classes. While the spherical AGB stars follow theoretical expectations of Mamon et al. (1988), the post-AGB structured outflow sources have significantly higher mass-loss rates than expected probably because of their recent superwinds. We find evidence that the structured outflows are clearly younger than the AGB wind and most likely begin at the end of the AGB or during the PPN stage of evolution. The disk sources have little correlation between mass-loss rate and envelope size, and their envelope lifetimes are significantly longer than expected for their envelope size. The molecular disk properties are determined more by the properties of the central stars and disk evolution than by the mass-loss rate history that shapes the spherical/elliptical/shell and the structured-outflow sources.

We are grateful for the financial support of several funding agencies. M. M. and A. Z. were partially supported by NSF CAREER grant AST 97-33697. D. F., M. M., E. C. S., and W. J. W. were partially supported by NSF grant AST 99-81546, the Laboratory of Astronomical Imaging at the University of Illinois, and the RAL at the University of California, Berkeley. M. M. was partially supported by STScI/DDRF grant D0001.82301. D. F. was partially supported by the Smithsonian Astrophysical Observatory. This research has made use of the SIMBAD database, operated at CDS, Strasbourg, France.

REFERENCES

Alcolea, J., & Bujarrabal, V. 1991, A&A, 245, 499
———. 1995, A&A, 303, L21
Alcolea, J., Bujarrabal, V., Sánchez Contreras, C., Neri, R., & Zweigle, J. 2001, A&A, 373, 932
Bachiller, R., Bujarrabal, V., Martin-Pintado, J., & Gomez-Gonzalez, J. 1989, A&A, 218, 252
Bachiller, R., Forveille, T., Huggins, P. J., Cox, P., & Maillard, J. P. 2000, A&A, 353, L5
Bachiller, R., Huggins, P. J., Cox, P., & Forveille, T. 1991, A&A, 247, 525
Bachiller, R., Huggins, P. J., Martin-Pintado, J., & Cox, P. 1992, A&A, 256, 231
Balick, B. 1987, AJ, 94, 671
Balick, B., Alexander, J., Hajian, A. R., Terzian, Y., Perinotto, M., & Patriarchi, P. 1998, AJ, 116, 360
Balick, B., & Frank, A. 2002, ARA&A, 40, 439
Bergman, P., Kerschbaum, F., & Olofsson, H. 2000, A&A, 353, 257
Bieging, J. H., Wilner, D., & Thronson, H. A. 1991, ApJ, 379, 271
Bieging, J. H., & Wilson, C. D. 2001, AJ, 122, 979
Bujarrabal, V., Alcolea, J., & Neri, R. 1998a, ApJ, 504, 915
Bujarrabal, V., Alcolea, J., & Planesas, P. 1992, A&A, 257, 701
Bujarrabal, V., Alcolea, J., Sahai, R., Zamorano, J., & Zijlstra, A. A. 1998b, A&A, 331, 361
Bujarrabal, V., Castro-Carrizo, A., Alcolea, J., & Neri, R. 2005, A&A, 441, 1031

Bujarrabal, V., Castro-Carrizo, A., Alcolea, J., & Sanchez-Contreras, C. 2001, A&A, 377, 868
Bujarrabal, V., Gomez-Gonzalez, J., Bachiller, R., & Martin-Pintado, J. 1988, A&A, 204, 242
Bujarrabal, V., Neri, R., Alcolea, J., & Kahane, C. 2003, A&A, 409, 573
Cahn, J. H. 1984, ApJ, 279, 304
Calvet, N., & Cohen, M. 1978, MNRAS, 182, 687
Castro-Carrizo, A., Bujarrabal, V., Fong, D., Meixner, M., Tielens, A. G. G. M, Latter, W. B., & Barlow, M. J. 2001a, A&A, 367, 674
Castro-Carrizo, A., Bujarrabal, V., Sánchez Contreras, C., Alcolea, J., & Neri, R. 2002, A&A, 386, 633
Castro-Carrizo, A., Bujarrabal, V., Sánchez Contreras, C., Sahai, R., & Alcolea, J. 2005, A&A, 431, 979
Castro-Carrizo, A., Lucas, R., Bujarrabal, V., Colomer, F., & Alcolea, J. 2001b, A&A, 368, L34
Cox, P., Huggins, P. J., Maillard, J.-P., Habart, E., Morisset, C., Bachiller, R., & Forveille, T. 2002, A&A, 384, 603
Cox, P., Lucas, R., Huggins, P. J., Forveille, T., Bachiller, R., Guilloteau, S., Maillard, J. P., & Omont, A. 2000, A&A, 353, L25
Crowther, P. A., de Marco, O., & Barlow, M. J. 1998, MNRAS, 296, 367
Dayal, A., & Bieging, J. H. 1995, ApJ, 439, 996
de Jager, C. 1998, A&A Rev., 8, 145
De Marco, O., Bond, H. E., Harmer, D., & Fleming, A. J. 2004, ApJ, 602, L93
Dyck, H. M., Benson, J. A., van Belle, G. T., & Ridgway, S. T. 1996, AJ, 111, 1705
Feast, M. W. 1996, MNRAS, 278, 11
Fernie, J. D. 1981, ApJ, 243, 576
Fernie, J. D., & Seager, S. 1995, PASP, 107, 853
Fong, D., Justtanont, K., Meixner, M., & Campbell, M. T. 2002, A&A, 396, 581
Fong, D., Meixner, M., Castro-Carrizo, A., Bujarrabal, V., Latter, W. B., Tielens, A. G. G. M., Kelly, D. M., & Sutton, E. C. 2001, A&A, 367, 652
Fong, D., Meixner, M., & Shah, R. Y. 2003, ApJ, 582, L39
Frank, A., & Blackman, E. G. 2004, ApJ, 614, 737
Gledhill, T. M., Chrysostomou, A., Hough, J. H., & Yates, J. A. 2001a, MNRAS, 322, 321
Gledhill, T. M., & Takami, M. 2001, MNRAS, 328, 266
Gledhill, T. M., Yates, J. A., & Richards, A. M. S. 2001b, MNRAS, 328, 301
Graham, J. R., Serabyn, E., Herbst, T. M., Matthews, K., Neugebauer, G., Soifer, B. T., Wilson, T. D., & Beckwith, S. 1993, AJ, 105, 250
Groenewegen, M. A. T. 1997, A&A, 317, 503
Groenewegen, M. A. T., & Ludwig, H.-G. 1998, A&A, 339, 489
Groenewegen, M. A. T., van der Veen, W. E. C. J., & Matthews, H. E. 1998, A&A, 338, 491
Hawkins, G. W., Skinner, C. J., Meixner, M. M., Jernigan, J. G., Arens, J. F., Keto, E., & Graham, J. R. 1995, ApJ, 452, 314
Helfer, T. T., Thornley, M. D., Regan, M. W., Wong, T., Sheth, K., Vogel, S. N., Blitz, L., & Bock, D. C.-J. 2003, ApJS, 145, 259
Helfer, T. T., Vogel, S. N., Lugten, J. B., & Teuben, P. J. 2002, PASP, 114, 350
Hirano, N., et al. 2004, ApJ, 616, L43
Hrivnak, B. J. 1995, ApJ, 438, 341
Hrivnak, B. J., Kwok, S., & Volk, K. M. 1989, ApJ, 346, 265
Huggins, P. J., Forveille, T., Bachiller, R., & Cox, P. 2000, ApJ, 544, 889
Huggins, P. J., & Healy, A. P. 1989, ApJ, 346, 201
Huggins, P. J., Olofsson, H., & Johansson, L. E. B. 1988, ApJ, 332, 1009
Jaminet, P. A., Danchi, W. C., Sutton, E. C., Bieging, J. H., Wilner, D., Russell, A. P. G., & Sandell, G. 1991, ApJ, 380, 461
Jørgensen, U. G., Hron, J., & Loidl, R. 2000, A&A, 356, 253
Josselin, E., & Lèbre, A. 2001, A&A, 367, 826
Josselin, E., Mauron, N., Planesas, P., & Bachiller, R. 2000, A&A, 362, 255
Jura, M., & Kahane, C. 1999, ApJ, 521, 302
Jura, M., Velusamy, T., & Werner, M. W. 2001, ApJ, 556, 408
Jura, M., & Werner, M. W. 1999, ApJ, 525, L113
Justtanont, K., Barlow, M. J., Skinner, C. J., & Tielens, A. G. G. M. 1992, ApJ, 392, L75
Justtanont, K., Skinner, C. J., Tielens, A. G. G. M., Meixner, M., & Baas, F. 1996, ApJ, 456, 337
Kahane, C., & Jura, M. 1996, A&A, 310, 952
Karovska, M., Hack, W., Raymond, J., & Guinan, E. 1997, ApJ, 482, L175
Kastner, J. H., Vrtilek, S. D., & Soker, N. 2001, ApJ, 550, L189
Kawabe, R., et al. 1987, ApJ, 314, 322
Kelly, D. M., & Latter, W. B. 1995, AJ, 109, 1320
Kerschbaum, F., Olofsson, H., Hron, J., & Lebzelter, T. 1997, Pulsating Stars—Recent Developments in Theory and Observation, 23rd Meeting of the IAU (Kyoto), Abstract
Kholopov, P. N. 1985, General Catalogue of Variable Stars, 4th ed.
Knapp, G. R., Bowers, P. F., Young, K., & Phillips, T. G. 1995, ApJ, 455, 293
Knapp, G. R., Dobrovolsky, S. I., Ivezić, Z., Young, K., Crosas, M., Mattei, J. A., & Rupen, M. P. 1999, A&A, 351, 97
Knapp, G. R., Jorissen, A., & Young, K. 1997, A&A, 326, 318
Knapp, G. R., & Morris, M. 1985, ApJ, 292, 640
Kwok, S., Volk, K. M., & Hrivnak, B. J. 1989, ApJ, 345, L51
Latter, W. B., Dayal, A., Bieging, J. H., Meakin, C., Hora, J. L., Kelly, D. M., & Tielens, A. G. G. M. 2000, ApJ, 539, 783
Latter, W. B., Hora, J. L., Kelly, D. M., Deutsch, L. K., & Maloney, P. R. 1993, AJ, 106, 260
Li, J., Harrington, J. P., & Borkowski, K. J. 2002, AJ, 123, 2676
Likkel, L. 1989, ApJ, 344, 350
Lindqvist, M., Olofsson, H., Lucas, R., Schöier, F. L., Neri, R., Bujarrabal, V., & Kahane, C. 1999, A&A, 351, L1
Liu, X.-W. 1997, in Proc. First *ISO* Workshop on Analytical Spectroscopy, ed. A. M. Heras et al. (ESA SP-419; Noordwijk: ESA), 87
Lorenz-Martins, S., & de Araujo, F. X. 1997, MNRAS, 291, 296
Loup, C., Forveille, T., Omont, A., & Paul, J. F. 1993, A&AS, 99, 291
Mamon, G. A., Glassgold, A. E., & Huggins, P. J. 1988, ApJ, 328, 797
Manchado, A., Guerrero, M. A., Stanghellini, L., & Serra-Ricart, M. 1996, The IAC Morphological Catalog of Northern Galactic Planetary Nebulae (La Laguna: IAC)
Masson, C. R., et al. 1985, ApJ, 292, 464
Mastrodemos, N., & Morris, M. 1998, ApJ, 497, 303
———. 1999, ApJ, 523, 357
Mauron, N., & Huggins, P. J. 1999, A&A, 349, 203
———. 2000, A&A, 359, 707
Meixner, M., Campbell, M. T., Welch, W. J., & Likkel, L. 1998, ApJ, 509, 392
Meixner, M., Skinner, C. J., Graham, J. R., Keto, E., Jernigan, J. G., & Arens, J. F. 1997, ApJ, 482, 897
Meixner, M., Ueta, T., Bobrowsky, M., & Speck, A. 2002, ApJ, 571, 936
Meixner, M., Young Owl, R., & Leach, R. W. 1999a, PASP, 111, 997
Meixner, M., Zalucha, A., Ueta, T., Fong, D., & Justtanont, K. 2004, ApJ, 614, 371
Meixner, M., et al. 1999b, ApJS, 122, 221
Molster, F. J., Waters, L. B. F. M., Tielens, A. G. G. M., & Barlow, M. J. 2002a, A&A, 382, 184
Molster, F. J., Waters, L. B. F. M., Tielens, A. G. G. M., Koike, C., & Chihara, C. 2002b, A&A, 382, 241
Nakashima, J.-I. 2005, ApJ, 620, 943
Neri, R., Kahane, C., Lucas, R., Bujarrabal, V., & Loup, C. 1998, A&AS, 130, 1
Ney, E. P., Merrill, K. M., Becklin, E. E., Neugebauer, G., & Wynn-Williams, C. G. 1975, ApJ, 198, L129
Olofsson, H., Bergman, P., Lucas, R., Eriksson, K., Gustafsson, B., & Bieging, J. H. 2000, A&A, 353, 583
Olofsson, H., Eriksson, K., Gustafsson, B., & Carlstroem, U. 1993, ApJS, 87, 305
Olofsson, H., Johansson, L. E. B., Hjalmarson, A., & Nguyen-Quang-Rieu, M. 1982, A&A, 107, 128
Omont, A., et al. 1995, ApJ, 454, 819
Planesas, P., Bachiller, R., Martin-Pintado, J., & Bujarrabal, V. 1990a, ApJ, 351, 263
Planesas, P., Kenney, J. D. P., & Bachiller, R. 1990b, ApJ, 364, L9
Reddy, B. E., & Hrivnak, B. J. 1999, AJ, 118, 1899
Regan, M. W., Thornley, M. D., Helfer, T. T., Sheth, K., Wong, T., Vogel, S. N., Blitz, L., & Bock, D. C.-J. 2001, ApJ, 561, 218
Reimers, D., & Cassatella, A. 1985, ApJ, 297, 275
Rodríguez, L. F., Goss, W. M., & Williams, R. 2002, ApJ, 574, 179
Sahai, R., Hines, D. C., Kastner, J. H., Weintraub, D. A., Trauger, J. T., Rieke, M. J., Thompson, R. I., & Schneider, G. 1998a, ApJ, 492, L163
Sahai, R., & Trauger, J. T. 1998, AJ, 116, 1357
Sahai, R., Wootten, A., Schwarz, H. E., & Wild, W. 1994, ApJ, 428, 237
Sahai, R., et al. 1998b, ApJ, 493, 301
Sanchez Contreras, C., Bujarrabal, V., & Alcolea, J. 1997, A&A, 327, 689
Sault, R. J., Staveley-Smith, L., & Brouw, W. N. 1996, A&AS, 120, 375
Sault, R. J., Teuben, P. J., & Wright, M. C. H. 1995, in ASP Conf. Ser. 77, Astronomical Data Analysis Software and Systems IV, ed. R. A. Shaw, H. E. Payne, & J. J. E. Hayes (San Francisco: ASP), 433
Schöier, F. L., Lindqvist, M., & Olofsson, H. 2005, A&A, 436, 633
Schöier, F. L., & Olofsson, H. 2001, A&A, 368, 969
Schöier, F. L., Ryde, N., & Olofsson, H. 2002, A&A, 391, 577
Schwarz, H. E., Aspin, C., Corradi, R. L. M., & Reipurth, B. 1997, A&A, 319, 267
Skinner, C. J., Meixner, M., & Bobrowsky, M. 1998, MNRAS, 300, L29
Skinner, C. J., Meixner, M. M., Hawkins, G. W., Keto, E., Jernigan, J. G., & Arens, J. F. 1994, ApJ, 423, L135
Skinner, C. J., et al. 1997, A&A, 328, 290

Soker, N. 2004, in ASP Conf. Ser. 313, Asymmetrical Planetary Nebulae III: Winds, Structure and the Thunderbird, ed. M. Meixner et al. (San Francisco: ASP), 562
———. 2005, AJ, 129, 947
Speck, A. K., Meixner, M., Fong, D., McCullough, P. R., Moser, D. E., & Ueta, T. 2002, AJ, 123, 346
Stanimirovic, S., Staveley-Smith, L., Dickey, J. M., Sault, R. J., & Snowden, S. L. 1999, MNRAS, 302, 417
Steer, D. G., Dewdney, P. E., & Ito, M. R, 1984, A&A, 137, 159
Steffen, M., & Schönberner, D. 2000, A&A, 357, 180
Szczerba, R., Omont, A., Volk, K., Cox, P., & Kwok, S. 1997, A&A, 317, 859
Thompson, R., et al. 1997, NASA and STScI Press Release PRC97-11
Truong-Bach, Nguyen-Q-Rieu, Morris, D., & Deguchi, S. 1990, A&A, 230, 431
Ueta, T., Meixner, M., & Bobrowsky, M. 2000, ApJ, 528, 861
Ueta, T., Speck, A. K., Meixner, M., Dayal, A., Hora, J. L., Fazio, G., Deutsch, L. K., & Hoffmann, W. F. 2001a, in Post-AGB Objects as a Phase of Stellar Evolution, 339
Ueta, T., et al. 2001b, ApJ, 557, 831
van Langevelde, H. J., van der Heiden, R., & van Schooneveld, C. 1990, A&A, 239, 193
Vogel, S. N., Wright, M. C. H., Plambeck, R. L., & Welch, W. J. 1984, ApJ, 283, 655
Waters, L. B. F. M., Waelkens, C., Mayor, M., & Trams, N. R. 1993, A&A, 269, 242
Weigelt, G., Balega, Y., Bloecker, T., Fleischer, A. J., Osterbart, R., & Winters, J. M. 1998, A&A, 333, L51
Welch, W. J., et al. 1996, PASP, 108, 93
Wong, T., & Blitz, L. 2002, ApJ, 569, 157
Young, K., Cox, P., Huggins, P. J., Forveille, T., & Bachiller, R. 1999, ApJ, 522, 387
Zweigle, J., Neri, R., Bachiller, R., Bujarrabal, V., & Grewing, M. 1997, A&A, 324, 624